



# UNIVERSITÀ DI PARMA

## ARCHIVIO DELLA RICERCA

University of Parma Research Repository

Dolostone pulverization induced by coseismic rapid decompression of CO<sub>2</sub>-rich gas in nature (Matese, Apennines, Italy)

This is the peer reviewed version of the following article:

*Original*

Dolostone pulverization induced by coseismic rapid decompression of CO<sub>2</sub>-rich gas in nature (Matese, Apennines, Italy) / Billi, A.; Smeraglia, L.; Aldega, L.; Balsamo, F.; Barberio, M. D.; Boschi, C.; Caracausi, A.; Carminati, E.; Iannace, A.; Mercuri, M.; Pizzati, M.; Tavani, S.. - In: EARTH AND PLANETARY SCIENCE LETTERS. - ISSN 0012-821X. - 604:(2023), p. 117996.117996. [10.1016/j.epsl.2023.117996]

*Availability:*

This version is available at: 11381/2952853 since: 2024-12-12T08:35:15Z

*Publisher:*

Elsevier

*Published*

DOI:10.1016/j.epsl.2023.117996

*Terms of use:*

Anyone can freely access the full text of works made available as "Open Access". Works made available

*Publisher copyright*

note finali coverpage

(Article begins on next page)

1 **Dolostone pulverization induced by coseismic rapid decompression of**  
2 **CO<sub>2</sub>-rich gas in nature (Matese, Apennines, Italy)**

3

4 Andrea Billi<sup>1\*</sup>, Luca Smeraglia<sup>1</sup>, Luca Aldega<sup>2</sup>, Fabrizio Balsamo<sup>3</sup>, Marino Domenico  
5 Barberio<sup>2</sup>, Chiara Boschi<sup>4</sup>, Antonio Caracausi<sup>5</sup>, Eugenio Carminati<sup>2</sup>, Alessandro Iannace<sup>6</sup>,  
6 Marco Mercuri<sup>2</sup>, Mattia Pizzati<sup>3</sup>, Stefano Tavani<sup>1,6</sup>

7

8 <sup>1</sup> Consiglio Nazionale delle Ricerche, IGAG, Rome, Italy.

9 <sup>2</sup> Department of Earth Sciences, Sapienza University of Rome, Italy.

10 <sup>3</sup> Department of Chemistry, Life Sciences and Environmental Sustainability, University of  
11 Parma, Italy.

12 <sup>4</sup> Consiglio Nazionale delle Ricerche, IGG, Pisa, Italy.

13 <sup>5</sup> Istituto Nazionale di Geofisica e Vulcanologia, Palermo, Italy.

14 <sup>6</sup> Dipartimento di Scienze della Terra, dell'Ambiente e delle Risorse, University of Naples,  
15 Italy.

16 \* corresponding author: Andrea Billi, Consiglio Nazionale delle Ricerche, IGAG, at  
17 Department of Earth Sciences, Sapienza University of Rome, Geochimica Building, P.le A.  
18 Moro 5, 00185, Rome, andrea.billi@cnr.it

19

20

21

## 22 **Abstract**

23 South Matese, Apennines, is a hydrothermally and seismically active extensional area  
24 characterized by CO<sub>2</sub> outgassing and Mw ≤7.1 earthquakes. There, meters-sized pockets  
25 of incohesive pulverized dolostone are hosted within Mesozoic carbonates at the hanging  
26 wall of seismically active normal faults. The aim of this paper is to understand the  
27 pulverization process. The pulverized dolostone is finely comminuted (down to a few  
28 microns), but primary structures, mainly bedding, are preserved. The grain size distribution  
29 is similar to that of previously studied pulverized rocks associated with active faults and  
30 dissimilar to that of carbonate cataclasites and fault gouges. The pulverized pockets are  
31 surrounded by zones (halos), in which the loose grains are cemented, in their original  
32 position, by microcrystalline calcite, resulting in a cemented micro-mosaic breccia. Stable  
33 isotopes from the cement are compatible with calcite precipitation from rapidly CO<sub>2</sub>-  
34 degassing shallow waters. Comparing our observations with results of laboratory  
35 experiments on carbonate pulverization through rapid decompression of pore-hosted CO<sub>2</sub>,  
36 the best explanation for the pulverized dolostone may lie on local accumulations of  
37 pressurized CO<sub>2</sub>-rich gas, suddenly decompressed during earthquakes. The limited  
38 permeability of the gas-saturated dolostone must have prevented a prompt escape of the  
39 gas from the rock, which was therefore anhydrously pulverized by the rapid expansion of  
40 the trapped gas. The sudden decompression must have suctioned bicarbonate-rich  
41 groundwaters, from which microcrystalline calcite rapidly precipitated, fossilizing the freshly  
42 pulverized dolostone. Calcite precipitation formed an impermeable shield around the  
43 pulverized pockets, which, therefore, remained internally uncemented. This process may  
44 have occurred over multiple cycles at depths shallower than the CO<sub>2</sub> subcritical–supercritical  
45 boundary (ca. -800 m). Although hypothetical, the proposed mechanism is for the first time  
46 suggested for an active tectonic environment. This case may improve our knowledge of

47 possible chemical-physical processes connected with the subsurface storage of CO<sub>2</sub> in  
48 seismically active areas.

49

## 50 **1. Introduction**

51 Pulverized rocks are extremely comminuted low-strain rocks in which the micro-clasts  
52 are almost in their original position such as to resemble a micro jigsaw puzzle. Pulverized  
53 rocks are typically found in low permeability rocks, such as crystalline or tight carbonate  
54 rocks, and even when these rocks occur within fault zones (as it usually happens), they are  
55 markedly different from cataclastic rocks and fault gouges in terms of grain size distribution,  
56 texture, and position within the deformation zone ([Brune, 2001](#); [Dor et al., 2006](#); [Rockwell  
57 et al., 2009](#); [Muto et al., 2015](#); [Schröckenfuchs et al., 2015](#); [Williams et al., 2021](#)). Due to  
58 these peculiar structural features and their occurrence within seismically active fault zones,  
59 pulverized rocks are often considered as diagnostic of coseismic high-strain-rate  
60 deformation within shallow (<3 km depth) confined rock volumes ([Wilson et al., 2005](#); [Doan  
61 and Gary, 2009](#); [Mitchell et al., 2011](#); [Yuan et al., 2011](#); [Sagy and Korngreen, 2012](#); [Rempe  
62 et al., 2013](#); [Aben et al., 2017b](#); [Fondriest et al., 2017](#); [Rodríguez-Escudero et al., 2020](#);  
63 [Ostermeijer et al., 2022](#)).

64 One interesting but poorly investigated mechanism of pulverization in active tectonic  
65 environments is the one connected with fluid (gas) pressure fluctuation within rocks. To this  
66 end, [Mitchell et al. \(2013\)](#) experimented with explosive pulverization of rocks by imparting  
67 rapid drops in gas confining pressure for noble gas-saturated rock samples (tonalite), using  
68 a specifically designed pressure vessel to allow near-instantaneous decompression of the  
69 rock samples. The limited permeability of the tested rocks created non-draining conditions  
70 during the rapid decompression experiments, resulting in the pulverization of the samples  
71 due to the sudden expansion of the gas trapped within the rock pores, unable to drain quickly  
72 from the rock ([Mitchell et al., 2013](#)). These promising laboratory experiments - recently  
73 substantiated by further similar experiments on carbonate using CO<sub>2</sub> as the rapidly  
74 expanding gas ([Hesse et al., 2022](#)) - were not validated on natural examples. Hence, the

75 pulverization mechanism via rapid decompression of gases within rocks remains  
76 experimentally operable but still elusive in nature, at least in active seismic domains.

77 We present a multidisciplinary study of pulverized dolostone exposed in the hanging  
78 wall of the south Matese normal fault system, Apennines, Italy ([Fig. 1a](#)). This site is ideal to  
79 study possible relationships between natural faulting, active fluid circulation, and rock  
80 pulverization in a seismically active region. The study area is indeed characterized by (1)  
81 seismically active normal faults ([Boncio et al., 2022](#)), (2) extensive exposure of dolostone,  
82 which is a rock type elsewhere documented to be often pulverized ([Agosta and Aydin, 2006](#);  
83 [Sagy and Korngreen, 2012](#); [Schröckenfuchs et al., 2015](#); [Fondriest et al., 2017](#); [Kaminskaite](#)  
84 [et al., 2020](#)), and (3) active circulation of CO<sub>2</sub>-rich fluids ([Figs. 1b and 1c](#)) that may partially  
85 derive from the nearby active or quiescent volcanic districts ([Di Luccio et al., 2018](#); [Santo et](#)  
86 [al., 2019](#)). Our main goal is to understand the mechanism of dolostone pulverization.

87

## 88 **2. Pulverization Models**

89 Although an increasing number of papers has been dedicated to this issue, no unique  
90 or broadly accepted explanations of how pulverized rocks form in nature are available ([Aben](#)  
91 [et al., 2017a](#); [Payne and Duan, 2017](#); [Ostermeijer et al., 2022](#)). To contextualize our results  
92 and establish the best model for the natural pulverization described in this work, we here  
93 provide a brief review of existing laboratory and numerical models for the genesis of  
94 pulverized rocks:

95 (1) Dynamic unloading: faulting along a bimaterial interface implies an abrupt  
96 reduction of normal stress at the fault tip. This produces a tensional wave that  
97 fractures the rock in fault-proximal domains in an event similar to a rock-burst due

98 to volumetric tensile expansion ([Ben-Zion and Shi, 2005](#); [Dor et al., 2006](#); [Payne](#)  
99 [and Duan, 2017](#)).

100 (2) Dynamic fragmentation: during very rapid coseismic strain rates, multiple  
101 fractures can propagate simultaneously before any appreciable stress is relieved.  
102 This process breaks the rock into fragments without shearing. Supershear faulting  
103 (when a fault rupture propagates faster than the shear wave speed) produces  
104 shock wave fronts that feature large changes in strain rate over a very small  
105 volume. As such, this mechanism is a good candidate for rock pulverization  
106 through dynamic fragmentation in fault-proximal domains ([Doan and Gary, 2009](#);  
107 [Doan and Billi, 2011](#); [Wechsler et al., 2011](#); [Yuan et al., 2011](#); [Doan and d'Hour,](#)  
108 [2012](#)).

109 (3) Transient tensile pulses: pulverized rocks found even 100 m away from the  
110 principal slip zone of seismogenic rupture can form during transient tensile stress  
111 perturbations created during the passage of earthquake ruptures. These ruptures  
112 and related stress perturbations are especially prevalent along bimaterial  
113 interfaces with a larger propensity to pulverization of stiffer and stronger rocks ([Xu](#)  
114 [and Ben-Zion, 2017](#); [Griffith et al., 2018](#); [Smith and Griffith, 2022a](#)).

115 (4) Rapid gas decompression: [Mitchell et al. \(2013\)](#) recorded an explosive  
116 pulverization mechanism within a laboratory setting by creating rapid drops in gas-  
117 confining pressure for gas-saturated (effectively unconfined) crystalline rock  
118 samples. Using a specifically designed pressure vessel that allows the  
119 instantaneous decompression of rock samples via a blow-out diaphragm, only  
120 low-permeability ( $10^{-19}$ - $10^{-20}$  m<sup>2</sup>) crystalline rocks were pulverized. This occurred  
121 through a sudden volumetric expansion driven by pore fluid where the confining  
122 pressure dropped faster than the pore pressure of the rock. The pulverized  
123 samples were characterized by non-systematically oriented pervasive

124 microfractures that bonded particles with size distribution from about 1 mm down  
125 to <0.01 mm. Recently, similar tests were performed by [Hesse et al. \(2022\)](#), who  
126 used commercial carbonate as the host rock and CO<sub>2</sub> as the pore-hosted gas. In  
127 a laboratory apparatus, the rock was permeated by CO<sub>2</sub> and both temperature  
128 and pressure were raised to supercritical CO<sub>2</sub> conditions. The rapid release of  
129 CO<sub>2</sub> into a decompression chamber resulted in an expansion of supercritical CO<sub>2</sub>  
130 inside the pores and consequent rock pulverization from tension. After three  
131 cycles of compression and rapid decompression, the carbonate samples were  
132 comminuted from 13.2 mm down to <300 μm particles.

133 In addition to the aforementioned models, coseismic processes predisposing rock to  
134 pulverization include the rapidly oscillating stresses during a single rupture potentially  
135 reducing the rock compressive strength ([Braunagel and Griffith, 2019](#)) or the occurrence of  
136 successive seismic high-strain rate loadings eventually leading to a reduction of the  
137 pulverization threshold ([Aben et al., 2016](#)).

138

### 139 **3. Geological Setting**

140 The studied exposure ([Figs. 1–3](#)) is located in the central-southern Apennines, a Late  
141 Oligocene to Present fold-thrust belt developed during the subduction of the Adriatic plate  
142 below the European one. Since the Early Pliocene, the internal (western) and axial parts of  
143 the central-southern Apennines belt have undergone post-orogenic exhumation and  
144 extensional faulting ([Malinverno and Ryan, 1986](#)). This extensional regime is still active and  
145 has generated a peri-Tyrrhenian volcanic system and a set of main NW-SE oriented  
146 extensional faults that are the source of Mw ≤7.1 historical and instrumental seismicity in the  
147 study area ([Galli and Naso, 2009](#); [Boncio et al., 2022](#)) as well as the main pathway of active



148 degassing ([Ascione et al., 2018](#)). We focused our study on the Ailano area, which is located  
149 at the south-western foot of the Matese Mts., on the hanging wall of the south Matese active  
150 normal fault system, nearby active or quiescent volcanic-hydrothermal districts ([Fig. 1](#)). In  
151 this area, the exposed stratigraphic sequence is characterized by Upper Triassic carbonate  
152 platform dolostone, upward followed by Lower Jurassic to Upper Cretaceous carbonate  
153 platform limestone and dolostone, and by syn-orogenic siliciclastic deposits ([Fig. 1a](#)). Based  
154 on the minimum thickness of the sedimentary pile previously overlying the study outcrop,  
155 we infer that the investigated area has been exhumed from a minimum depth of about 3.5  
156 km. Obviously, this depth does not necessarily represent the depth of dolostone  
157 pulverization.

158 In the study area, the main fault system is extensional, NW-striking, SW-dipping, and  
159 it occurs toward the NE. The investigated area is therefore located on a wide and fractured-  
160 faulted hanging wall block ([Fig. 1a](#)). The subsurface structural architecture of this hanging  
161 wall block is substantially unknown. Due to the presence of numerous active normal faults  
162 and associated degassing vents in the study area, we hypothesize, however, the presence  
163 of a set of fluid-conductive active normal fault zones beneath and in the vicinity of the studied  
164 exposure (see the cross-section in [Fig. 1a](#)), where outcrop-scale faults are directly observed  
165 ([Fig. 2a](#)).

166 In the study area, CO<sub>2</sub>- and CH<sub>4</sub>-rich (up to 30.000 g x d<sup>-1</sup> and 2000 g x d<sup>-1</sup>  
167 respectively; [Ascione et al., 2018](#)) gas vents and large diffusive gas emissions from soil  
168 occur close to the villages of Ciorlano and Ailano ([Fig. 1](#)), with mantle-derived fluids (e.g.,  
169 CO<sub>2</sub>, helium) that are involved in the local seismicity (e.g., [Caracausi and Paternoster, 2015](#);  
170 [Di Luccio et al., 2018](#)). The helium isotopic signature is between 0.7 and 1 Ra ([Fig. 1c](#), [Table](#)  
171 [S1](#); [Caracausi and Paternoster, 2015](#); [Ascione et al., 2018](#); unpublished INGV data), larger  
172 than typical crustal fluid values (0.01–0.03 Ra) from cratons and sedimentary basins far from

173 active tectonic regions (Fig. 1c). Fig. 1(c) clearly indicates that He in the Ailano-Ciorlano  
174 gases results from a mixing of mantle and crustal components, where the high flux of  
175 volatiles at the surface has been hypothesized as being driven by the presence of magmatic  
176 melts at depth beneath the Matese region (Italiano et al., 2000; Di Luccio et al., 2018).

177

## 178 **4. Methods**

179 We collected data and rock samples (Table S2) along a ~200 m long road cut, where  
180 fractured Lower Jurassic platform carbonates and discrete zones/pockets of pulverized  
181 carbonates are exposed (Figs. 2 and 3; Lat. 41.397729°, Long. 14.171114°). We combined  
182 the following analytical techniques on both the pulverized and the host rocks: outcrop-scale  
183 geological and structural observations and analyses; thin section analysis under optical  
184 microscope and associated cathodoluminescence, and under scanning electronic  
185 microscope (SEM) and associated Energy Dispersive Spectrometry (EDS); grain size  
186 distribution analyses: 2D image analysis and 3D laser diffraction granulometry on  
187 cohesive/impregnated and incohesive samples, respectively; X-ray diffraction analyses;  
188 geochemical analyses of major and minor elements and rare earth elements (REE); and  
189 carbon and oxygen stable isotope analyses. All methods are described in detail in the  
190 [Supplemental Material](#).

191

## 192 **5. Results**

### 193 **5.1 Field Observations**

194 Along the studied exposure, we recognized two main types of rocks relevant to our  
195 research (Figs. 2, 3, and S1-S5): (1) cohesive host carbonates (mainly dolostone) displaying

196 bedding and (2) pockets of incohesive pulverized carbonates (mainly dolostone) hosted  
197 within the bedded carbonates. We differentiate distal and proximal cohesive host rocks  
198 based on the distance from the incohesive pulverized pockets (distal: >10 m; proximal: <20  
199 cm). An angular unconformity marked by overlying Quaternary breccias truncates the upper  
200 part of the exposure, made of pulverized dolostone and bedded carbonates (Fig. 2b).

201 The host rock consists of decimeters-thick beds of dolostone and dolomitic limestone  
202 as well as rarer limestone that are fractured and faulted (Fig. 2a). The beds are NE-dipping  
203 by about 45°. Fractures are very frequent (fracture spacing is often about 1 cm or less) and  
204 hardly systematic, although main sets include fractures striking NW–SE and dipping toward  
205 either NE or SW by about 70° or more. Faults (only 17 along the study exposure) are less  
206 frequent than joints and with very limited displacement (less than a few centimeters). Fault  
207 surfaces strike preferentially NW–SE, with a dip angle of about 60°, either toward NE or  
208 toward SW. A set of faults, N–S striking and dipping toward E by about 70°, is also present  
209 (Fig. 2a; Table S3).

210 The incohesive pulverized pockets are meters-sized and characterized by irregular  
211 or chimney/domal morphologies. Pulverized dolostone is usually white in color, totally  
212 incohesive, very fine-grained, and shows jagged or transitional to sharp boundaries with the  
213 fractured host rock (Figs. 2 and 3; Videos S1-S4; Virtual Outcrops S1-S4). In many cases,  
214 primary bedding is still visible within the pulverized pockets (Figs. 2b-2d and 3a; Video S4).  
215 Pebble-shaped fragments of the host rock are occasionally found within the fine-grained  
216 matrix of the pulverized dolostone (Fig. 3b). The domal pockets of pulverized dolostone  
217 appear, in some cases, upwardly bounded by a thin (2–5 cm) layer of shale or clayey marl  
218 occurring along the bedded host dolostone. At least in one case, the shale layer has an  
219 antiformal geometry around the upper portion of a domal pocket of pulverized rocks (Fig.  
220 3e).

221

## 222 **5.2 Microscopic Observations**

223 The distal and proximal host rocks are characterized by a large variety of  
224 depositional/diagenetic microstructures, which are usually well preserved (Fig. 4). In the  
225 distal host rock (Fig. 4a-c), primary depositional features are perfectly preserved together  
226 with intergranular early phreatic cements and late diagenetic blocky calcite (Fig. 4a). Fine-  
227 grained crystalline dolomites display an excellent preservation of the grainstone depositional  
228 texture (Fig. 4b). In places, incomplete replacement of limestone by dolomite is recorded  
229 (Fig. 4b). A zoned and coarse crystalline dolomite within fractures and cavities and  
230 poikilotopic calcite occur (Fig. 4c), probably representing hydrothermal dolomitization.  
231 These depositional and diagenetic features are typical of Upper Triassic-Lower Jurassic  
232 shallow water carbonates from the central Apennine carbonate platform (Iannace et al.,  
233 2011).

234 Under optical microscope, the proximal host rock surrounding and embedding the  
235 pulverized carbonates is characterized by alternating dark and light concentric bands (Figs.  
236 4d and 4e) consisting of a mosaic of fine-grained dolomite crystals showing equal grain sizes  
237 (Figs. 4e and 4f). The former sedimentary structures are perfectly decipherable within the  
238 banded zones (Figs. 4c and 4d). The fine-grained dolostone crystals are non-luminescent  
239 (Figs. 4g, 4h, and S4a–S4f) and, in places, are cut by <1 mm thick microfractures filled by  
240 blocky calcite crystals showing a dull red and zoned luminescence color (Figs. 4g and 4h).

241 SEM observations, together with EDS analyses, revealed that dolomite (of both distal  
242 and proximal host rocks) consists of fine-grained crystals (Figs. 5a–5c, S1, and S2). In  
243 places, dolomite crystal boundaries are visible (Figs. 5a, 5b, and S1), while in other cases,  
244 crystals are well welded (Figs. 5c and S1). Intergranular porosity occurs between the

245 crystals (Figs. 5a–5c, S1e-S1h, and S3a). Occasionally, calcite-filled veins crosscut the fine-  
246 grained dolomite crystals (Figs. 5a and S2c–S2e).

247 SEM observations further reveal the micro-texture of the proximal cohesive host rock,  
248 which consists of grains immersed in a microcrystalline calcite cement, each grain being  
249 formed by single crystals or more often by aggregates of dolomite crystals. The resulting  
250 pattern is a cemented micro mosaic or crackle-like breccia (Fig. 5e-5i, S2c-S2h, S3b, S3c,  
251 and S5b). The microcrystalline calcite cement displays a dominant black color under  
252 cathodoluminescence, with rare bright orange rims along the outer crystal edges (Fig. S4e  
253 and S4f). No substantial shear displacement is observed along the microfractures (i.e.  
254 between the grains), which are non-systematically oriented and mostly coincide with the  
255 crystal (or crystal–aggregate) boundaries. The dolomite crystals contain widespread  
256 micropores (Figs. 5e, 5f, S1f–S1h, S3a, and S3b). Crystal boundaries are generally sharp;  
257 however, in places, these boundaries may be rounded or with embayment-like morphologies  
258 (Figs. 5e, 5f, S2c, and S2d). The transition toward bands dominated by microcrystalline  
259 calcite cement is diffuse and is characterized by dolomite crystals fading within the calcite  
260 cement (Figs. 5f and S2d). Small, rounded pockets of fine grained (pulverized) dolomite  
261 grains also occur (Figs. 5h, 5i, and S2e-S2g). In these pockets, no calcite cement is present  
262 while, in contrast, calcite cement is present all around them. Occasionally, <100 µm thick  
263 calcite filled veins cut across the dolomite crystals (Figs. 5g, 5i, and S2g).

264 At the micro-scale, pulverized incohesive carbonates sampled within the pulverized  
265 pockets consist of dolostone grains with sharp boundaries (Figs. 5k, 5l, S2h, and S3d). The  
266 rhombohedral habit of dolostone crystals is still preserved, although the crystal faces are  
267 often characterized by small cavities (Figs. 5k-l and S3d). The dolostone grains consist of  
268 single crystals or, in places, crystal aggregates (Fig. 5k). As a synthesis of our micro-

269 observations, [Fig. S5](#) shows a micro-comparison between incohesive pulverized dolostone  
270 and cohesive distal and proximal host rocks.

271

### 272 **5.3 Grain Size Distributions**

273 The incohesive pulverized dolostone (dolostone grains from pulverized pockets; [Figs.](#)  
274 [5k and 5l](#)) were analyzed both through the 3D method (laser granulometry) and through the  
275 2D image analysis method (on SEM photomicrographs using epoxy-impregnated samples;  
276 e.g. [Fig. 5k](#)) whereas the cohesive host rocks (dolostone in [Figs. 5a-5c](#) and cemented  
277 mosaic breccias in [Figs. 5d–5f](#)) only through the 2D method. All grain size distributions are  
278 unimodal and well sorted. Results are as follows ([Fig. 6](#)).

279 Distal host rocks: grain sizes are between 2 and 90  $\mu\text{m}$  in diameter (coinciding with  
280 the size of dolomite crystals); mean grain diameters are between 10.5 and 47.8  $\mu\text{m}$ , with  
281 modal values of distribution curves between 5.2 and 11.2  $\mu\text{m}$  ([Fig. 6a](#))

282 Proximal host rocks (mosaic microbreccias): the grain size distributions are  
283 comprised between 4 and 200  $\mu\text{m}$  in diameter (coinciding mainly with the size of dolomite  
284 crystals and to a lesser extent with the size of crystal aggregates); mean grain diameters  
285 are between 66.3 and 86.1  $\mu\text{m}$  with modal values of distribution curves falling between 18.7  
286 and 31.1  $\mu\text{m}$  ([Fig. 6b](#)). The shift towards coarser grain size fraction can be related to the  
287 presence of polycrystalline aggregates.

288 Pulverized dolostone (2D image analysis): grain size distribution curves are  
289 comprised between 8 and 1100  $\mu\text{m}$  in diameter; mean grain diameters are between 247.4  
290 and 786.8  $\mu\text{m}$ , with modal values of distribution curves between 18.7 and 41.1  $\mu\text{m}$  ([Fig. 6c](#)).  
291 Higher values of average diameters are due to the occurrence of mm-size crystal  
292 aggregates (e.g. [Fig. 5k](#)).

293 Pulverized dolostone (3D laser granulometry analysis): grain size distributions fall  
294 between 1 and ~2000  $\mu\text{m}$  in diameter; mean grain diameters are between 57.8 and 153  $\mu\text{m}$ ,  
295 with modal values of distribution curves between 42.9 and 106  $\mu\text{m}$  (Fig. 6d).

296 SEM observations on the incohesive or impregnated pulverized dolostone show that  
297 the grains are made up of individual dolomite crystals of 20–30  $\mu\text{m}$  in size or by dolomite  
298 crystal aggregates spanning from 70–90  $\mu\text{m}$  up to 1500  $\mu\text{m}$  (Figs. 5k, 5l, S3d, and S20-22).  
299 All results from grain size analyses are summarized in Tables S4 and S5 and in Figs. S6–  
300 S22.

301

#### 302 **5.4 Bulk X-Ray Diffraction**

303 We performed X-ray semiquantitative analyses of the bulk composition of eleven  
304 samples from the cohesive host rock (proximal and distal), ten samples from the incohesive  
305 pulverized dolostone, and three samples from the shale or clayey marl occurring along the  
306 bedded host rock (Fig. 7 and Table S6). The distal host carbonates include two  
307 endmembers: the first one is characterized by prevailing dolomite (between 91 and 93%)  
308 and low calcite contents (7–9%), and the second one is entirely composed of calcite (99%)  
309 with very low dolomite content, not exceeding 1% (Fig. 7). Samples from the proximal host  
310 rock show variable amounts of dolomite, in the range of 63 to 98% (average 81%), and  
311 calcite, between 2 and 37% (average 19%; Fig. 7). The pulverized rocks show greater  
312 amounts of dolomite (from 85 to 100%, average 98%) and smaller amounts of calcite (from  
313 0 to 10%, average 2%; Fig. 7) than their counterparts in the host rock. Occasionally, sheet  
314 silicates occur in the pulverized rocks, with contents lower than 6% (Fig. 7). In a few  
315 pulverized samples, traces of norsethite  $\text{BaMg}(\text{CO}_3)_2$ , a mineral belonging to the dolomite  
316 group, occur. Shale interbedded with dolostone layers contain sheet silicates (mica, chlorite,

317 and kaolinite) with amounts ranging between 70 and 89%, calcite (6–24%), hematite (2–  
318 4%), and minor amounts of quartz (1–2%) and dolomite (1–2%) (Fig. 7). Traces of gypsum  
319 were observed in the X-ray tracings (Supplemental Diffractograms).

320

### 321 **5.5 Bulk and Punctual Analyses of Stable Isotopes**

322 Stable isotope analyses show that both proximal and distal host rocks and pulverized  
323 dolostone are characterized by similar values of  $\delta^{13}\text{C}$  and  $\delta^{18}\text{O}$  (Fig. 8a and Table S7). We  
324 acknowledge that these results refer to bulk analysis (i.e., without separating dolomite and  
325 calcite components in the samples). In particular,  $\delta^{13}\text{C}$  values show a narrow range,  
326 between +2.5 ‰ and +4.0 ‰ V-PDB, whereas  $\delta^{18}\text{O}$  values range between +28.0 ‰ and  
327 +33.0 ‰ V-SMOW (Fig. 8a). Such values are typical for most marine carbonates, particularly  
328 the Jurassic-Cretaceous ones in the central Apennines (e.g., Agosta and Kirschner, 2003).

329 We also performed punctual stable isotope analyses on a set of micro subsamples  
330 that were collected along four centimeter-scale transects across banded calcite with  
331 dolomite grains in cohesive proximal host rocks (see the analyzed samples in Fig. S23).  
332 Similar banded calcite is visible nearby cemented mosaic breccias also in Figs. 5d, 5f, and  
333 S2d. The  $\delta^{18}\text{O}_{\text{calcite}}$  values show a narrow range, between +26.0 ‰ and +28.0 ‰, whereas  
334 the  $\delta^{13}\text{C}_{\text{calcite}}$  values show a wide range, between +3.0 ‰ and +8.0 ‰ (see calcite transects  
335 in Figs. 8a and 8b). The  $\delta^{18}\text{O}_{\text{dolomite}}$  values show a range between +31.0 ‰ and +37.0 ‰,  
336 whereas, similarly to  $\delta^{13}\text{C}_{\text{calcite}}$ , the  $\delta^{13}\text{C}_{\text{dolomite}}$  values show a wider range, between +3.0 ‰  
337 and +8.0 ‰ (see dolomite transects in in Figs. 8a).

338

### 339 **5.6 Bulk Analysis of REE and Minor Chemical Elements**



340 Bulk analyses (i.e., without separating dolomite and calcite components in the  
341 samples) of REE (rare Earth elements) and minor chemical elements from (distal and  
342 proximal) host rocks and pulverized dolostone show similar patterns (Figs. 8c and 8d, Table  
343 S8). In particular, minor element concentration spans from 0.01 ppm to 1,000 ppm. The  
344 abundance of REE in pulverized dolostone and host rocks shows large variations, ranging  
345 from 0.002 ppm to 0.025 ppm. No anomalous concentrations were observed (Figs. 8c and  
346 8d).

347 The PAAS-normalized (Post-Archean Australian Shales) patterns show that the REE  
348 concentrations in the host rock and in the pulverized dolostone are in the range that is typical  
349 for the Mesozoic carbonates in the central Apennines (Fig. 8d; Castorina et al. 2020). Most  
350 samples show a negative Ce anomaly (Fig. 8d), typical of marine carbonates, and La/Sm  
351 and La/Yb ratios  $<1$  (Fig. 8d), typical of carbonate rocks in late diagenetic conditions (Fig.  
352 8d).

353

## 354 **6. Discussion**

### 355 **6.1 Pulverized Rocks**

356 The first issue to be discussed is whether the studied rocks are truly pulverized rocks  
357 (*sensu* Brune, 2001 and Dor et al., 2006) or otherwise cataclasites or fault gouges. The  
358 following features suggest a pulverized nature of the studied rocks: (1) the very fine grained  
359 and unimodal size distribution of clasts is similar to those of previously studied pulverized  
360 rocks (Muto et al., 2015; Schröckenfuchs et al., 2015; Williams et al., 2021; Hesse et al.,  
361 2022) and dissimilar to those of polymodal and poorly sorted cataclastic rocks and fault  
362 gouges (Reches and Dewers, 2005; Cortinovia et al., 2019; Fig. 9); (2) the distribution in  
363 discrete pockets (Fig. 2) is very different from the typical occurrence of fault-parallel and

364 proximal (often tabular) bands of cataclastic rocks and fault gouges (e.g. [Reches and](#)  
365 [Dewers, 2005; Williams et al., 2021](#)); and (3) the preservation of primary structures, such as  
366 bedding, within the pulverized pockets ([Figs. 2b-2d and 3a](#)) is typical of all pulverized rocks  
367 so far studied (e.g. [Ostermeijer et al., 2022](#), and references therein). Indeed, these latter  
368 structures, together with the cemented micro-mosaic breccias ([Figs. 5d–5f](#)) surrounding the  
369 incohesive pulverized rocks, show that the pulverized dolostone was essentially shattered  
370 in situ without significant clast rotations, translations, and shear, as documented for many  
371 previously studied pulverized rocks ([Dor et al., 2006; Ostermeijer et al., 2022](#)). Moreover,  
372 pulverized rocks, both from dolostone ([Fondriest et al., 2017](#)) and from crystalline rocks  
373 ([Rempe et al., 2013; Rodríguez-Escudero et al., 2020](#)), are usually characterized by non-  
374 systematically oriented micro-fractures separating the single grains. A non-systematic  
375 pattern of fractures separating the single grains is also visible in the micro-mosaic breccias  
376 studied in this work ([Figs. 5e and 5f](#)).

377

## 378 **6.2 Pulverization and Cementation**

379 To understand the pulverization process, we start from some main observations. The  
380 pulverized dolostone is entirely incohesive and surrounded by a rock halo, i.e. the proximal  
381 host rock, which consists of cemented micro-mosaic breccias. The perfect preservation of  
382 details of the sedimentary features clearly indicates that the rocks suffered intense  
383 microfracturing with minimal strain. Moreover, the perfect polygonal fitting of dolomite clasts  
384 indicates that they are almost in their original position ([Figs. 5d–5f](#)) and the related grain  
385 size distribution is very similar to that of the incohesive pulverized dolostones apart from a  
386 few coarse-grained aggregates ([Fig. 5k](#); compare the modal peaks of [Figs. 6b-6d](#)). Hence,  
387 it seems reasonable to infer that the pulverization process was predominantly anhydrous  
388 and was soon after followed by arrival of mineralizing fluids with rapid calcite cementation in

389 the proximal zones, fossilizing the pulverized grain pattern and forming a low permeability  
390 cohesive shield (halo) around the incohesive pulverized dolostone. The banded pattern, in  
391 places, of the calcite cement (Fig. S23) may indicate successive cycles of cement growth,  
392 but we cannot determine the rate (rapid vs. slow) of successive band development.  
393 Repeated cycles of pulverization and post-pulverization cementation may have also  
394 occurred, but we have no clear clues to identify them.

395 The host rock is very heterogeneous, with varying amounts of calcite and dolomite  
396 constituting the two endmembers (Fig. 7). Therefore, we cannot infer whether the  
397 pulverization process chemically altered one of the endmembers (calcite and dolomite);  
398 however, the incohesive pulverized pockets are almost entirely made up of dolomite  
399 (average content = 98%; Fig. 7). This evidence suggests that pulverization affected almost  
400 pure dolostone, as previously observed elsewhere in faulted carbonates (Fondriest et al.,  
401 2017). Since, in fact, the pulverization process often operates by breaking apart the crystal  
402 boundaries (inter- rather than intra-crystalline fractures; Doan and Billi, 2011), the  
403 microcrystalline texture of (sedimentary) limestone can prevent the pulverization itself (e.g.  
404 dilation breccias in limestone; Tarasewicz et al., 2005) due to an excessive energy  
405 necessary to break apart every microcrystalline boundary, whereas the macrocrystalline  
406 pattern of many dolostones is more prone to pulverization (Fondriest et al., 2017;  
407 Kaminskaite et al., 2020). The same applies to the macrocrystalline (Carrara) marble (Doan  
408 and Billi, 2011).

409 In the same way as the X-ray diffraction, also bulk geochemical analyses (i.e., where  
410 the calcite cement was not separated by the host rock) do not allow us to identify sharp  
411 differences in minor elements or REE between the analyzed rocks (Fig. 8c and 8d). Yet, the  
412 punctual isotope analyses on the calcite cement show a different pattern with respect to the  
413 rest of the analyzed samples (Figs. 8a and 8b). In particular, the reduced values of  $\delta^{18}\text{O}$

414 (around 27 ‰ instead of 30 ‰ V-SMOW) and the increasing values of  $\delta^{13}\text{C}$  (from 3 ‰ to  
415 almost 8 ‰ V-PDB) for the calcite cement analyzed in samples A1.1, A1.1bis, A1.3, and  
416 A4.2 (Figs. 8a, 8b, and S23) are compatible with a trend of isotope fractionation of carbon  
417 dissolved in water during calcite cement precipitation from a parent solution that rapidly  
418 degassed  $\text{CO}_2$  (Baldermann et al., 2020). Di Luccio et al. (2018) found similar carbon isotope  
419 values (from 3 to 8 ‰ V-PDB) in active springs in the Matese area and ascribed this pattern  
420 to  $\text{CO}_2$ -degassed waters possibly containing a deep  $\text{CO}_2$  contribution. Fig. 8(a) shows that,  
421 similarly to calcite, also the dolomite contained in samples A1.1bis, A1.3, and A4.2 is  
422 characterized by an interval of  $\delta^{13}\text{C}$  values from 3 to almost 8 ‰ V-PDB. This pattern may  
423 indicate an isotopic re-equilibration of dolomite grains pervaded by the above-mentioned  
424 water solution that rapidly degassed  $\text{CO}_2$ , precipitating the calcite cement.

425

### 426 **6.3 Hypotheses and Implications**

427 As explained in Section 2, it is not yet known how pulverized rocks form naturally  
428 (Aben et al., 2017a; Payne and Duan, 2017; Ostermeijer et al., 2022) and, consequently,  
429 any correlation between natural pulverized rocks and potential genetic models is rather  
430 speculative, including ours as follows. In particular, considering the main genetic models  
431 explained in Section 2, we believe that the first three (dynamic unloading, dynamic  
432 fragmentation, and rapidly oscillating stresses during a single rupture) could be excluded for  
433 the pulverized dolostone studied in this paper as these models are used to explain large  
434 masses of fault-proximal pulverized rocks often occurring along bimaterial interfaces. On the  
435 contrary, the pulverized dolostone studied in this paper occurs in meters-sized discrete  
436 pockets far away from major fault surfaces. Consequently, the best guess we can make  
437 relates to the rapid gas decompression model (see Section 2), which would explain why the

438 pulverized dolostone occurs in meters-sized discrete pockets rather than in larger amasses  
439 adjacent to faults.

440 The above-mentioned structural and geochemical evidence, particularly the fact that  
441 the studied pulverized pockets are completely incohesive and surrounded by a halo of  
442 cemented micro-mosaic breccias, suggests us that the process of pulverization must have  
443 been somehow driven mainly by gases and related pressure fluctuations. In fact, if the  
444 system would have been dominated by CO<sub>2</sub>-rich groundwaters, we would probably also  
445 have had calcite pervasive precipitation within the pulverized pockets. We therefore  
446 hypothesize that the dolostone pulverization was mainly driven by gas pocket accumulations  
447 and related pressure fluctuations within restricted volumes of rocks prone to be pulverized  
448 for their internal structure (see rapid gas decompression in Section 2). This hypothesis is  
449 supported by the large output of deeply-sourced CO<sub>2</sub>-rich gases in the study area ([Italiano  
450 et al., 2000](#); [Caracausi and Paternoster, 2015](#); [Di Luccio et al., 2018](#); [Ascione et al., 2019](#)).  
451 Moreover, the frequent occurrence of clay-rich layers at the top of the pulverized pockets  
452 ([Fig. 3e](#)) suggests that the gas may have accumulated in what are now the pulverized  
453 pockets, in part due to the sealing effect exerted by the clay-rich layers.

454 Thus, the aforementioned pulverization process by rapid decompression of the gas  
455 trapped in the rock ([Mitchell et al., 2013](#); [Hesse et al., 2022](#)) becomes a valid candidate to  
456 explain the formation of the studied rocks. Such a process would involve a rapid expansion  
457 of a pore-trapped gas (unable to quickly drain out of the rock) due to a rapid decompression  
458 and consequent micro-fragmentation of the host rock (pulverization). We believe that the  
459 sudden gas decompression may have been triggered by one of the discussed coseismic  
460 models or processes predisposing rock to pulverization (see Section 2). For instance, we  
461 suppose the transient tensile pulses that may occur 100 m or even further away from the  
462 principal slip zone of seismogenic rupture (e.g., [Bhat et al., 2012](#); [Xu and Ben-Zion, 2017](#);

463 [Griffith et al., 2018](#); [Smith and Griffith, 2022b](#)); however, we have no reliable clues as to  
464 what mechanism could have caused the sudden decompression.

465 The following evidence further supports the hypothesis of a pulverization driven by  
466 gas pressure changes. The dolomitic host rock has a primary intergranular microporosity  
467 ([Figs. 5a–5c](#)). This microporosity may have generated the appropriate level of permeability  
468 suitable to host the gas inside (through a slow saturation) but sufficiently low to prevent its  
469 escape during rapid decompression events. [Mitchell et al. \(2013\)](#) demonstrated that  
470 pulverization through rapid decompression of gas-saturated rocks can occur solely when  
471 intermediate-low permeability values allow sufficient rock saturation by the gas but hinder  
472 any rapid escape of the gas itself. Moreover, our micro-observations and grain size  
473 distribution analyses demonstrated that the pulverization process occurred mainly because  
474 of inter- rather than intra-crystalline fracturing ([Figs. 5e and 5f](#)). Intergranular porosity may  
475 have been decisive in localizing fractures between single crystals (interfaces between  
476 adjacent crystals) or crystal aggregates. We infer that the energy that suddenly involved the  
477 studied rocks (rapid gas expansion) was not sufficient to further break the rocks themselves  
478 and tear apart every single crystal from its neighbors or even fragment the single crystals  
479 with intra-crystalline fractures. Note also that the resulting mean grain size of the pulverized  
480 dolostone is compatible with the mean size range of previously studied fault-related  
481 pulverized rocks (e.g., [Schrockenfuchs et al., 2015](#); [Williams et al., 2021](#)), including the fine-  
482 grained material obtained after three cycles of CO<sub>2</sub> decompression by [Hesse et al. \(2022\)](#)  
483 ([Fig. 9](#)). In [Fig. 9](#), note that the grain size data by [Hesse et al. \(2022\)](#) have a lower boundary  
484 around 100 μm connected with the method of analysis (i.e., sieving).

485 The CaCO<sub>3</sub>-cements that fossilized the micro-mosaic breccias around the pulverized  
486 pockets is microcrystalline and equigranular, and such a breccia is known to develop  
487 impulsively ([Melosh et al., 2014](#)). Hence, a reasonable hypothesis is that this cement too

488 formed impulsively soon after the pulverization. An explanation may be that rapidly  
489 decompressed and pulverized pockets suctioned, due to the difference in pressure, nearby  
490 bicarbonate-rich waters from which microcrystalline calcite rapidly precipitated in the  
491 decompressed and pulverized pockets, consistently with the Sibson's suction pump model  
492 ([Sibson, 1987](#), [Smeraglia et al., 2016](#), and [Brantut, 2020](#)). The isotope data discussed above  
493 ([Figs. 8a and 8b](#)) support the precipitation of the calcite cement from a CO<sub>2</sub>-degassed  
494 groundwater. Such a precipitation would have quickly formed a low permeability halo or  
495 shield around the incohesive pockets, which would therefore have remained protected from  
496 further mineralizing fluids. These sealing halos formed not only at the outcrop-scale but also  
497 at the micro-scale ([Figs. 5h and 5i](#)). The same type of sealing halo was also found in  
498 coseismic micro-scale pulverized and cemented carbonates along the Mt. Morrone fault (see  
499 figure S2d in [Coppola et al., 2021](#)). A shielding role (i.e. protecting the pulverized rocks from  
500 mineralizing fluids) may have been played also by the outward expansion of pressurized  
501 CO<sub>2</sub> right after its sudden decompression.

502         The model of pulverization by rapid decompression of gas-saturated rocks proposed  
503 by [Mitchell et al. \(2013\)](#) and [Hesse et al. \(2022\)](#) implies a disruptive event necessary to  
504 suddenly lower the pore pressure in the rock. We hypothesize that this type of disruptive  
505 event may have been an earthquake. The study area is highly seismic ([Boncio et al., 2022](#))  
506 and the relationship between rock pulverization and high-energy earthquakes has been  
507 previously proposed ([Ostermeijer et al., 2022](#), and [references therein](#)). Using the words by  
508 [Rowe and Griffith \(2015\)](#): “At high strain rates, the transition from discrete fracture to  
509 pulverization is governed by the rate sensitivity of fracture toughness, adding evidence that  
510 rock pulverization is a true signature of high strain rate deformation that can only be achieved  
511 during earthquake rupture or extraterrestrial impacts ([Bhat et al., 2012](#)).” However, in our  
512 study case, a cause–effect relationship between earthquakes and dolostone pulverization



513 is speculative and should be further investigated and validated. At present, no more  
514 plausible causes than an earthquake can be proposed for the sudden decompression of the  
515 studied rocks. To this end, as mentioned above, it is noteworthy that some structures  
516 observed around the pulverized pockets were also observed in coseismic microlayers along  
517 the Mt. Morrone fault in the central Apennines (compare [Figs. 5h and 5i](#) in this work with  
518 figure S2d in [Coppola et al., 2021](#)). More in general, microcrystalline calcite precipitation  
519 along faults in different tectonic regimes can be one immediate effects of earthquake-related  
520 stress drop (e.g. [Bouiller et al., 2004](#); [Smeraglia et al., 2018](#)). However, we cannot exclude  
521 that the rapid decompression was generated by the sudden breaking of a permeability  
522 barrier due to the accumulation of pressurized fluids itself or to the energy radiated by a  
523 nearby volcanic eruption.

524

#### 525 **6.4 Possible model**

526 [Fig. 10](#) synthesizes our hypothetical view of the studied pulverization process:

- 527 (1) During interseismic phases, CO<sub>2</sub>-rich gases accumulated at the top of a  
528 bicarbonate-rich aquifer in meters-sized pockets of dolostone that is characterized  
529 by primary intergranular porosity. The gas was provided by deep sources (crust  
530 and mantle) at local and regional scale (e.g. [Caracausi and Paternoster, 2015](#); [Di  
531 Luccio et al., 2018](#)).
- 532 (2) During disruptive events - likely high-energy seismic events - the gas underwent  
533 rapid decompression. Where the permeability was sufficiently low to prevent a  
534 prompt escape of the gas from the rock, the sudden expansion of the trapped gas  
535 within the rock pores pulverized the rock itself.
- 536 (3) Shortly after the pulverization, the decompression as well as and the permeability  
537 increase enhanced by the failure of intercrystalline boundaries suctioned the



538 nearby bicarbonate-saturated waters toward the pulverized pockets, where rapid  
539 cementation of the pulverized rock occurred due to microcrystalline calcite  
540 precipitation (Sibson, 1987). The rapid cementation formed a low permeability  
541 halo around the inner portion of the pulverized dolostone, which therefore  
542 remained substantially uncemented, at least in the most internal portion.

543

#### 544 **6.5 Hypothetical depth and time of pulverization**

545 Although we have no certain constraints to adequately infer the depth of pulverization,  
546 tectono-stratigraphic data suggest that the outcrop studied should not have undergone a  
547 burial depth deeper than a few kilometers (~3.5 km). Similar to what was previously  
548 suggested for pulverized rocks exposed elsewhere, we believe that pulverization occurred  
549 at shallower burial conditions (Yuan et al., 2011). If our hypothesis of pulverization driven by  
550 rapid decompression of CO<sub>2</sub>-rich gases is viable, then this process should have  
551 preferentially occurred above the boundary between the subcritical gaseous CO<sub>2</sub> (above)  
552 and the supercritical CO<sub>2</sub> (midway between a gas and a liquid; below) identified by many  
553 studies at approximately 800 m depth (van der Meer et al., 2009). The rapid decompression  
554 model implies indeed a rapid expansion that is a property of gases and not liquids.  
555 Considering this depth limit (800 m), we can further speculate on the age of the pulverization  
556 process by considering the average exhumation rate of 0.5 mm/yr that seems valid for most  
557 parts of the Apennines (Erlanger et al., 2022 and references therein). By multiplying this rate  
558 with the hypothetical maximum depth of 800 m for the pulverization process, we obtain a  
559 hypothetical maximum age of 400 ka for the pulverized rocks. This age matches the period  
560 of main eruptive activities in the nearby Roccamonfina Volcano (between 439 ± 9 and 148  
561 ± 9 ka; Rouchon et al., 2008), which may have been the main source of CO<sub>2</sub> in the studied

562 area, thus strengthening our hypothesis of dolostone pulverization linked with gas venting  
563 and rapid decompression in the shallow crust.

564

## 565 **7. Conclusions**

566 Evidence from the southwestern margin of the Matese Mts. allows us to hypothesize  
567 a new mechanism for dolostone natural pulverization, which has never been proposed in  
568 natural active tectonic environments. This mechanism implies gas (CO<sub>2</sub>) saturation of rock  
569 during the interseismic phase and coseismic rapid decompression that makes the gas  
570 rapidly expand within the rock, thus pulverizing the host rock in situ. As shown by previous  
571 laboratory experiments, this mechanism can only work when there are appropriate intervals  
572 of permeability that hinder the rapid escape of the gas from the rock. We believe that this  
573 mechanism should be further explored, documented, and validated elsewhere before being  
574 considered as a viable process of (coseismic) deformation in active tectonic environments.  
575 It is, however, a process to consider when operating subsurface CO<sub>2</sub> storage. A rapid  
576 decompression of the stored CO<sub>2</sub> may indeed dramatically shatter the host rock, change its  
577 physical properties, and even promote the CO<sub>2</sub> escape outside the reservoir.

578

## 579 **Acknowledgements**

580 We acknowledge no funding for this study except the ordinary institutional ones (i.e.  
581 from authors' institutions; e.g. Fondi di Ateneo 2021 to E. Carminati). We thank A. Webb  
582 and an anonymous reviewer for their useful suggestions. A. Billi thanks T. Mitchell for  
583 sharing his original idea of pulverization through the rapid gas decompression. We kindly  
584 thank B. Klein and M. Hesse for providing the grain size distribution raw data of their  
585 experimentally pulverized rocks.

586

587

588 **References**

- 589 Aben, F.M., Doan, M.-L., Mitchell, T.M., Toussaint, R., Reschla, T., Fondriest, M., Gratier,  
590 J.-P., Renard, F., 2016. Dynamic fracturing by successive coseismic loadings leads  
591 to pulverization in active fault zones. *Journal of Geophysical Research*, 121, 2338–  
592 23360
- 593 Aben, F.M., Doan, M.-L., Gratier, J.-P., Renard, F., 2017a. Coseismic damage generation  
594 and pulverization in fault zones: Insights from dynamic Split-Hopkinson Pressure Bar  
595 experiments. In: *Fault zone dynamic processes: evolution of fault properties during*  
596 *seismic rupture*, edited by: Thomas, M. Y., Mitchell, T. M., and Bhat, H. S.,  
597 *Geophysical Monograph*, John Wiley & Sons, Inc.
- 598 Aben, F.M., Doan, M.-L., Gratier, J.-P., Renard, F., 2017b. High strain rate deformation of  
599 porous sandstone and the asymmetry of earthquake damage in shallow fault zones.  
600 *Earth and Planetary Science Letters*, 463, 81–91.
- 601 Agosta, F., Kirschner, D.L., 2003. Fluid conduits in carbonate-hosted seismogenic normal  
602 faults of central Italy. *Journal of Geophysical Research*, 108, 2221,  
603 doi:10.1029/2002JB002013.
- 604 Agosta, F., Aydin, A., 2006. Architecture and deformation mechanism of a basin bounding  
605 normal fault in Mesozoic platform carbonates, Central Italy. *Journal of Structural*  
606 *Geology*, 28, 1445-1467.
- 607 Ascione, A., Ciotoli, G., Bigi, S., Buscher, J., Mazzoli, S., Ruggiero, L., Sciarra, A., Tartarello,  
608 M.C., Valente, E., 2018. Assessing mantle versus crustal sources for non-volcanic  
609 degassing along fault zones in the actively extending southern Apennines mountain  
610 belt (Italy). *Geological Society of America Bulletin*, 130, 1697–1722.
- 611 Baldermann, A., Mittermayr, F., Bernasconi, S.M., Dietzel, M., Grengg, C., Hippler, D.,  
612 Kluge, T., Leis, A., Lin, K., Wang, X., Zünterl, A., Boch, R., 2020. Fracture dolomite  
613 as an archive of continental palaeo-environmental conditions. *Communications Earth*  
614 *& Environment*, 1, 35, <https://doi.org/10.1038/s43247-020-00040-3>
- 615 Ben-Zion, Y., Shi, Z., 2005. Dynamic rupture on a material interface with spontaneous  
616 generation of plastic strain in the bulk. *Earth and Planetary Science Letters*, 236, 486-  
617 496.
- 618 Bhat, H.S., Rosakis, A.J., Sammis, C.G., 2012. A micromechanics based constitutive model  
619 for brittle failure at high strain rates. *Journal of Applied Mechanics*, 79, 031016,
- 620 Boncio, P., Auciello, E., Amato, V., Aucelli, P., Petrosino, P., Tangari, A.C., Jicha, B., 2022.  
621 Late Quaternary faulting in the southern Matese (Italy): implications for earthquake  
622 potential and slip rate variability in the southern Apennines. *Solid Earth*, 13, 553–582.
- 623 Boullier, A.M., Fujimoto, K., Ohtani, T., Roman-Ross, G., Lewin, E., Ito, H., Pezard, P.,  
624 Ildefonse, B., 2004. Textural evidence for recent co-seismic circulation of fluids in the  
625 Nojima fault zone, Awaji island, Japan. *Tectonophysics*, 378, 165-181.
- 626 Brantut, N., 2020. Dilatancy-induced fluid pressure drop during dynamic rupture: Direct  
627 experimental evidence and consequences for earthquake dynamics. *Earth and*  
628 *Planetary Science Letters*, 538, 116179.

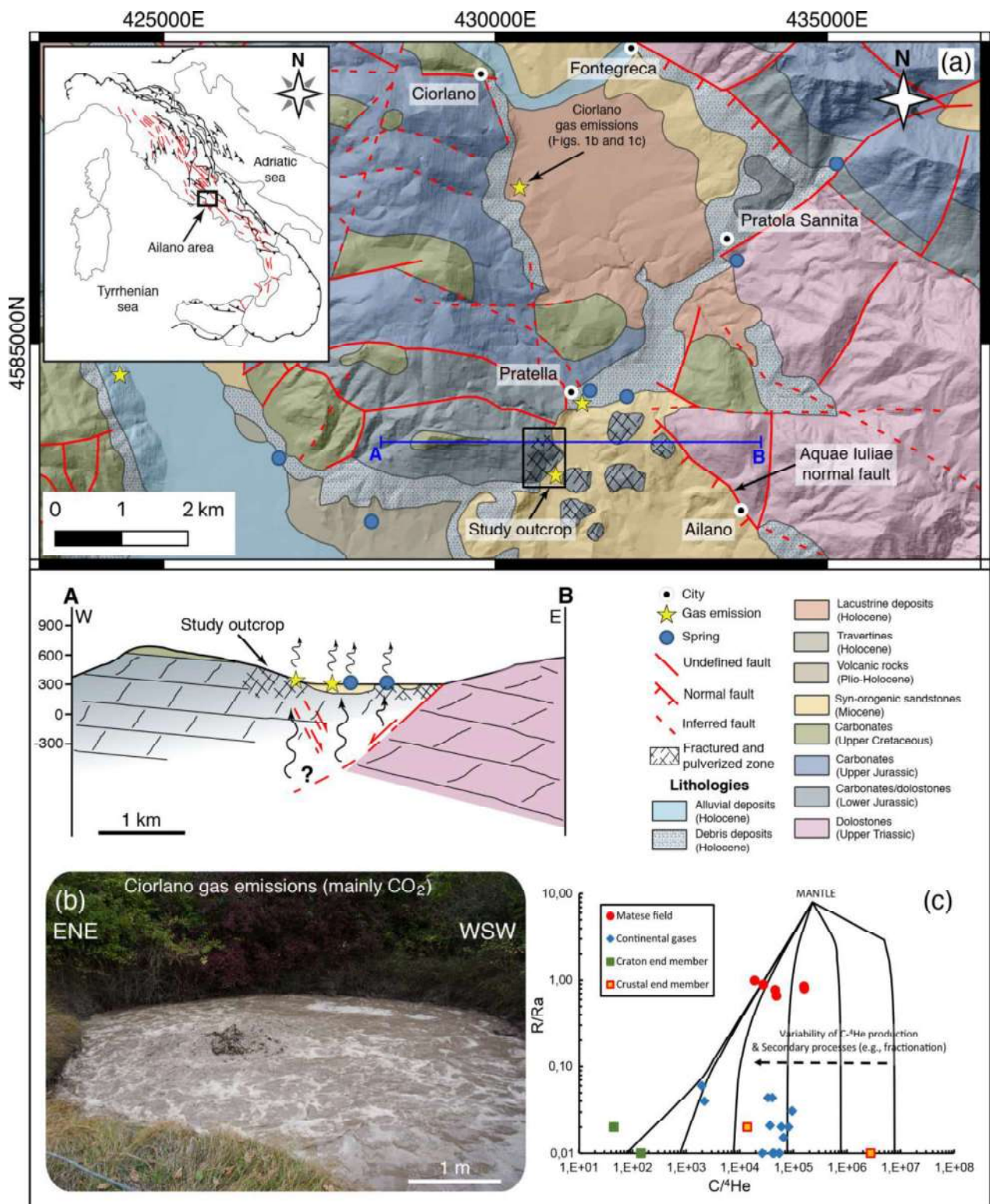
- 629 Braunagel, M.J., Griffith, W.A., 2019. The effect of dynamic stress cycling on the  
630 compressive strength of rocks. *Geophysical Research Letters*, 46, 6479–6486.
- 631 Brune, J.N., 2001. Fault normal dynamic loading and unloading: an explanation for “non-  
632 gouge” rock powder and lack of fault-parallel shear bands along the San Andreas  
633 fault. *EOS Trans. Am. Geophys. Union*, 82.
- 634 Caracausi, A., Paternoster, M., 2015. Radiogenic helium degassing and rock fracturing: A  
635 case study of the southern Apennines active tectonic region. *Journal of Geophysical  
636 Research*, 120, 2200-2211, doi:10.1002/2014JB011462.
- 637 Castorina, F., Masi, U., Billi, A., 2020. Assessing the origin of Sr and Nd isotopes and (REE+  
638 Y) in Middle-Upper Pleistocene travertines from the Acquasanta Terme area  
639 (Marche, central Italy) and implications for neotectonics. *Applied Geochemistry*, 117,  
640 104596.
- 641 Coppola, M., Correale, A., Barberio, M.D., Billi, A., Cavallo, A., Fondriest, M., Nazzari, M.,  
642 Paonita, A., Romano, C., Stagno, V., Viti, C., Vona, A., 2021. Meso- to nano-scale  
643 evidence of fluid-assisted co-seismic slip along the normal Mt. Morrone Fault, Italy:  
644 implications for earthquake hydrogeochemical precursors. *Earth and Planetary  
645 Science Letters*, 568, 117010, <https://doi.org/10.1016/j.epsl.2021.117010>.
- 646 Cortinovis, S., Balsamo, F., Storti, F., 2019. Influence of analytical operating procedures on  
647 particle size distributions in carbonate cataclastic rocks. *Journal of Structural  
648 Geology*, 128, 103884, <https://doi.org/10.1016/j.jsg.2019.103884>
- 649 Di Luccio, F., Chiodini, G., Caliro, S., Cardellini, C., Convertito, V., Pino, N.A., Tolomei, C.,  
650 Ventura, G., 2018. Seismic signature of active intrusions in mountain chains. *Science  
651 Advances*, 4, e1701825.
- 652 Doan, M.-L., Gary, G., 2009. Rock pulverization at high strain rate near the San Andreas  
653 fault. *Nature Geoscience*, 2, 709–712.
- 654 Doan, M.-L., Billi, A., 2011. High strain rate damage of Carrara marble. *Geophysical  
655 Research Letters*, 38, L19302, <https://doi.org/10.1029/2011GL049169>
- 656 Doan, M.-L., D'Hour, V., 2012. Effect of initial damage on rock pulverization along faults.  
657 *Journal of Structural Geology*, 45, 113-124, doi:10.1016/j.jsg.2012.05.006
- 658 Dor, O., Ben-Zion, Y., Rockwell, T.K., Brune, J., 2006. Pulverized rocks in the Mojave  
659 section of the San Andreas Fault Zone. *Earth and Planetary Science Letters*, 245,  
660 642–654.
- 661 Erlanger, E.D., Fellin, M.G., Willett, S.D., 2022. Exhumation and erosion of the Northern  
662 Apennines, Italy: new insights from low-temperature thermochronometers. *Solid  
663 Earth*, 13, 347–365, <https://doi.org/10.5194/se-13-347-2022>
- 664 Fondriest, M., Doan, M.L., Aben, F., Fousseis, F., Mitchell, T.M., Voorn, M., Secco, M., Di  
665 Toro, G., 2017. Static versus dynamic fracturing in shallow carbonate fault zones.  
666 *Earth and Planetary Science Letters*, 461, 8–19.
- 667 Galli, P.A.C., Naso, J.A., 2009. Unmasking the 1349 earthquake source (southern Italy):  
668 paleoseismological and archaeoseismological indications from the Aquae Iuliae fault.  
669 *Tectonophysics*, 31, 128-149, <https://doi.org/10.1016/j.jsg.2008.09.007>
- 670 Griffith, W.A., St. Julien, R.C., Ghaffari, H.O., Barber, T.J., 2018. A tensile origin for fault  
671 rock pulverization. *Journal of Geophysical Research*, 123, 7055–7073.

- 672 Hesse, M., Asetre, P., Anderson, R., Edwards, C., Lee, C., Malpica, O., Klein, B., 2022.  
673 Experimental demonstration of comminution with transcritical carbon dioxide cycles.  
674 Powder Technology, 407, 117615, <https://doi.org/10.1016/j.powtec.2022.117615>.
- 675 Iannace, A., Capuano, M., Galluccio, L., 2011. “Dolomites and dolomites” in Mesozoic  
676 platform carbonates of the Southern Apennines: Geometric distribution, petrography  
677 and geochemistry. Palaeogeography, Palaeoclimatology, Palaeoecology, 310, 324-  
678 339.
- 679 Italiano, F., Martelli, M., Martinelli, G., & Nuccio, P. M. (2000). Geochemical evidence of melt  
680 intrusions along lithospheric faults of the Southern Apennines, Italy: geodynamic and  
681 seismogenic implications. Journal of Geophysical Research: Solid Earth, 105(B6),  
682 13569-13578.
- 683 Kaminskaite, I., Fisher, Q.J., Michie, E.A.H., 2020. Faults in tight limestones and dolostones  
684 in San Vito lo Capo, Sicily, Italy: internal architecture and petrophysical properties.  
685 Journal of Structural Geology, 132, 103970.
- 686 Malinverno, A., Ryan, W.B., 1986. Extension in the Tyrrhenian Sea and shortening in the  
687 Apennines as result of arc migration driven by sinking of the lithosphere. Tectonics,  
688 5, 227-245.
- 689 Melosh, B.L., Rowe, C.D., Smit, L., Groenewald, C., Lambert, C.W., Macey, P., 2014. Snap,  
690 Crackle, Pop: Dilational fault breccias record seismic slip below the brittle–plastic  
691 transition. Earth and Planetary Science Letters, 403, 432-445.
- 692 Mitchell, T.M., Ben-Zion, Y., Shimamoto, T., 2011. Pulverized fault rocks and damage  
693 asymmetry along the Arima Takatsuki Tectonic Line, Japan. Earth and Planetary  
694 Science Letters, 308, 284–297.
- 695 Mitchell, T.M., Billi, A., Miller, S.A., Goldsby, D.L., Scholz, C.H., Gran, J. K., Simons, J.,  
696 2013. Dynamic pulverization by rapid decompression. Eos Transactions AGU, Fall  
697 Meeting Supplement, Abstract MR41B–04.
- 698 Mostardini, F., Merlini, S., 1986. Appennino centro meridionale. Sezioni geologiche e  
699 proposta di modello strutturale. Memorie della Società Geologica Italiana, 35, 177-  
700 202.
- 701 Muto, J., Nakatani, T., Nishikawa, O., Nagahama, H., 2015. Fractal particle size distribution  
702 of pulverized fault rocks as a function of distance from the fault core. Geophysical  
703 Research Letters, 42, 3811–3819, <https://doi.org/10.1002/2015GL064026>
- 704 Orr, F.M., 2009. Onshore Geologic Storage of CO<sub>2</sub>. Science, 325, 1656-1658.
- 705 Ostermeijer, G.A., Aben, F.M., Mitchell, T.M., Rockwell, T.K., Rempe, M., Farrington, K.,  
706 2022. Evolution of co-seismic off-fault damage towards pulverization. Earth and  
707 Planetary Science Letters, 579, 117353.
- 708 Payne, R.M., Duan, B., 2017. Insights into pulverized rock formation from dynamic rupture  
709 models of earthquakes. Geophysical Journal International, 208, 715–723,  
710 <https://doi.org/10.1093/gji/ggw436>.
- 711 Reches, Z., Dewers, T.A., 2005. Gouge formation by dynamic pulverization during  
712 earthquake rupture. Earth and Planetary Science Letters, 235, 361-374.

- 713 Rempe, M., Mitchell, T., Renner, J., Nippres, S., Ben-Zion, Y., Rockwell, T., 2013. Damage  
714 and seismic velocity structure of pulverized rocks near the San Andreas Fault, *Journal*  
715 *of Geophysical Research*, 118, 2813–2831.
- 716 Rockwell, T., Sisk, M., Girty, G., Dor, O., Wechsler, N., Ben-Zion, Y., 2009. Chemical and  
717 physical characteristics of pulverized Tejon Lookout granite adjacent to the San  
718 Andreas and Garlock Faults: implications for earthquake physics. *Pure and Applied*  
719 *Geophysics*, 166, 1725–1746.
- 720 Rodríguez-Escudero, E., Martínez-Díaz, J.J., Giner-Robles, J.L., Tsige, M., Cuevas-  
721 Rodríguez, J., 2020. Pulverized quartz clasts in gouge of the Alhama de Murcia fault  
722 (Spain): Evidence for coseismic clast pulverization in a matrix deformed by frictional  
723 sliding. *Geology*, 48, 283–287.
- 724 Rouchon, V., Gillot, P.Y., Quidelleur, X., Chiesa, S., Floris, B., 2008. Temporal evolution of  
725 the Roccamonfina volcanic complex (Pleistocene), Central Italy. *Journal of*  
726 *Volcanology and Geothermal Research*, 177, 500-514.
- 727 Rowe, C.D., Griffith, W.A., 2015. Do faults preserve a record of seismic slip: A second  
728 opinion. *Journal of Structural Geology*, 78, Pages 1-26
- 729 Santo, A., Santangelo, N., Balassone, G., Strauss, H., 2019. Deep seated fault-related  
730 volcanogenic H<sub>2</sub>S as the key agent of high sinkhole concentration areas. *Earth*  
731 *Surface Processes and Landforms*, 44, 713–735.
- 732 Sagy, A., Korngreen, D., 2012. Dynamic branched fractures in pulverized rocks from a deep  
733 borehole. *Geology*, 40, 799–802.
- 734 Schröckenfuchs, T., Bauer, H., Grasemann, B., Decker, K., 2015. Rock pulverization and  
735 localization of a strike-slip fault zone in dolomite rocks (Salzach–Ennstal–Mariazell–  
736 Puchberg fault, Austria). *Journal of Structural Geology*, 78, 67–85.
- 737 Sibson, R.H., 1987. Earthquake rupturing as a mineralizing agent in hydrothermal systems.  
738 *Geology*, 15, 701-704.
- 739 Smeraglia, L., Berra, F., Billi, A., Boschi, C., Carminati, E., Doglioni, C., 2016. Origin and  
740 role of fluids involved in the seismic cycle of extensional faults in carbonate rocks.  
741 *Earth and Planetary Science Letters*, 450, 292-305.
- 742 Smeraglia, L., Bernasconi, S.M., Berra, F., Billi, A., Boschi, C., Caracausi, A., Carminati, E.,  
743 Castorina, F., Doglioni, C., Italiano, F., Rizzo, A.L., Uysal, T., Zhao, J.-x., 2018.  
744 Crustal-scale fluid circulation and co-seismic shallow comb-veining along the longest  
745 normal fault of the central Apennines, Italy. *Earth and Planetary Science Letters*, 498,  
746 152-168.
- 747 Smith, Z.D., Griffith, W.A., 2022a. Evolution of pulverized fault zone rocks by dynamic tensile  
748 loading during successive earthquakes. *Geophysical Research Letters*,  
749 <https://doi.org/10.1029/2022GL099971>
- 750 Smith, Z.D., Griffith, W.A., 2022b. Lithological controls on fault damage zone development  
751 by coseismic tensile loading. *Tectonophysics*, 838, 229471,  
752 <https://doi.org/10.1016/j.tecto.2022.229471>.
- 753 Tarasewicz, J.P.T., Woodcock, N.H., Dickson, J.A.D., 2005. Carbonate dilation breccias:  
754 examples from the damage zone to the Dent Fault, northwest England. *Geological*  
755 *Society of America Bulletin*, 117, 736-745.

- 756 van der Meer, L.G.H., Hofstee, C., Orlic, B., 2009. The fluid flow consequences of CO<sub>2</sub>  
757 migration from 1000 to 600 metres upon passing the critical conditions of CO<sub>2</sub>. *Energy*  
758 *Procedia*, 1, 3213–3220.
- 759 Yuan, F., Prakash, V., Tullis, T., 2011. Origin of pulverized rocks during earthquake fault  
760 rupture. *Journal of Geophysical Research*, 116, B06309, doi:  
761 10.1029/2010JB007721.
- 762 Wechsler, N., Allen, E.E., Rockwell, T.K., Girty, G., Chester, J.S., Ben-Zion, Y., 2011.  
763 Characterization of pulverized granitoids in a shallow core along the San Andreas  
764 Fault, Littlerock, CA, *Geophysical Journal International*, 186, 401–417.
- 765 Williams, R.T., Rowe, C.D., Okamoto, K., Savage, H.M., Eves, E., 2021. How fault rocks  
766 form and evolve in the shallow San Andreas fault. *Geochemistry, Geophysics,*  
767 *Geosystems*, 22, e2021GC010092, <https://doi.org/10.1029/2021GC010092>
- 768 Wilson, B., Dewers, T., Reches, Z., Brune, J., 2005. Particle size and energetics of gouge  
769 from earthquake rupture zones. *Nature*, 434, 749–752.
- 770 Xu, S., Ben-Zion, Y., 2017. Theoretical constraints on dynamic pulverization of fault zone  
771 rocks. *Geophysical Journal International*, 209, 282–296,  
772 <https://doi.org/10.1093/gji/ggx033>.
- 773





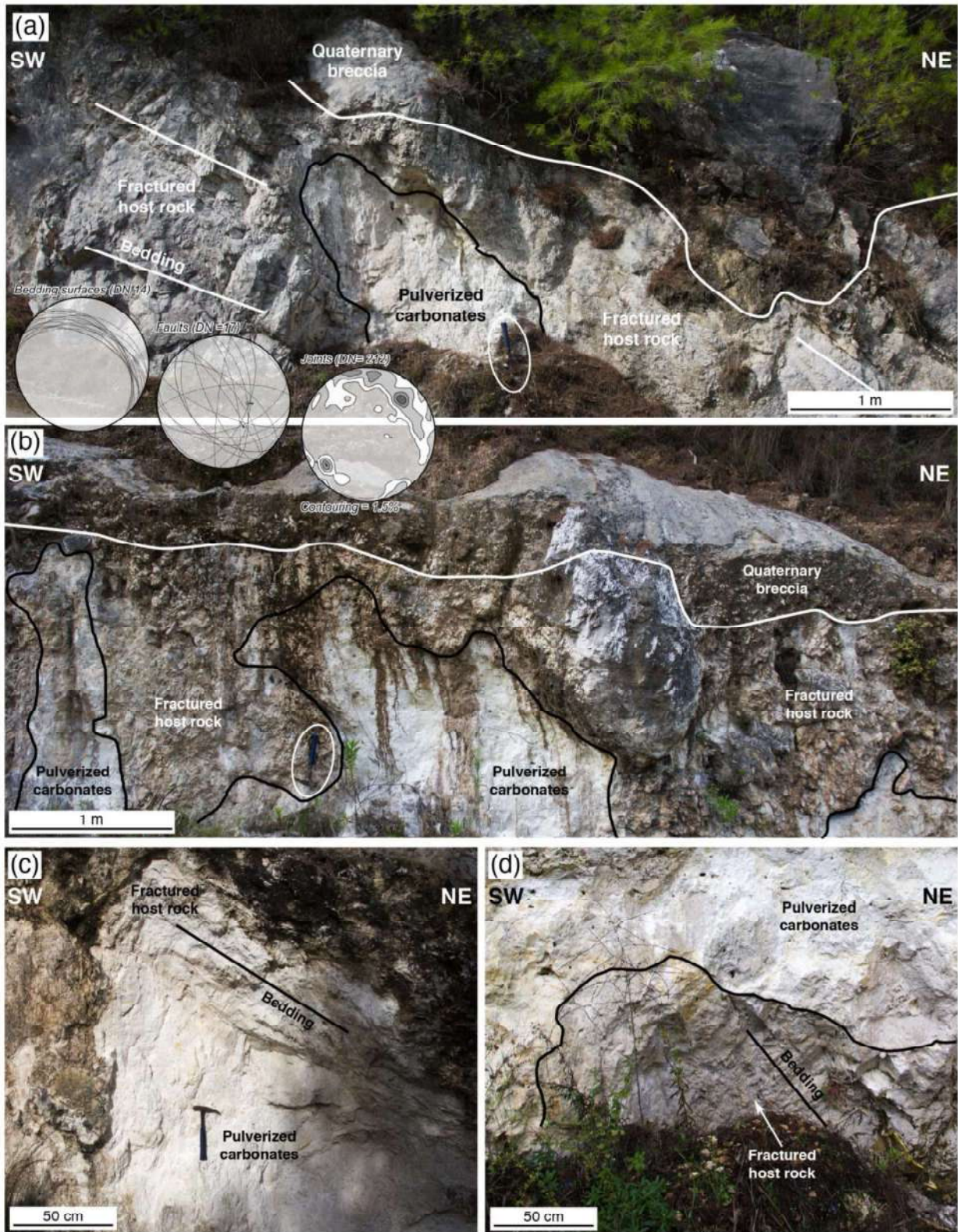
731

732 **Figure 1.** Geological setting. (a) Geological setting of the study area. Inset shows location  
 733 of the study area in Italy, wherein red faults are main active normal faults and black faults  
 734 are main thrusts. See, below the map, a geological cross-section through the study area,  
 735 showing that the studied exposure is located at the hanging wall of a normal fault system

736 with active CO<sub>2</sub>-rich springs and vents. **(b)** Photograph of the Ciorlano active CO<sub>2</sub>-rich spring  
737 nearby the studied rock exposure (see the map for its location). **(c)** Geochemical data from  
738 the Ciorlano spring and nearby springs (see the Hydrothermal Setting section for further  
739 information). Data plotted in this diagram are in Table S1.

740





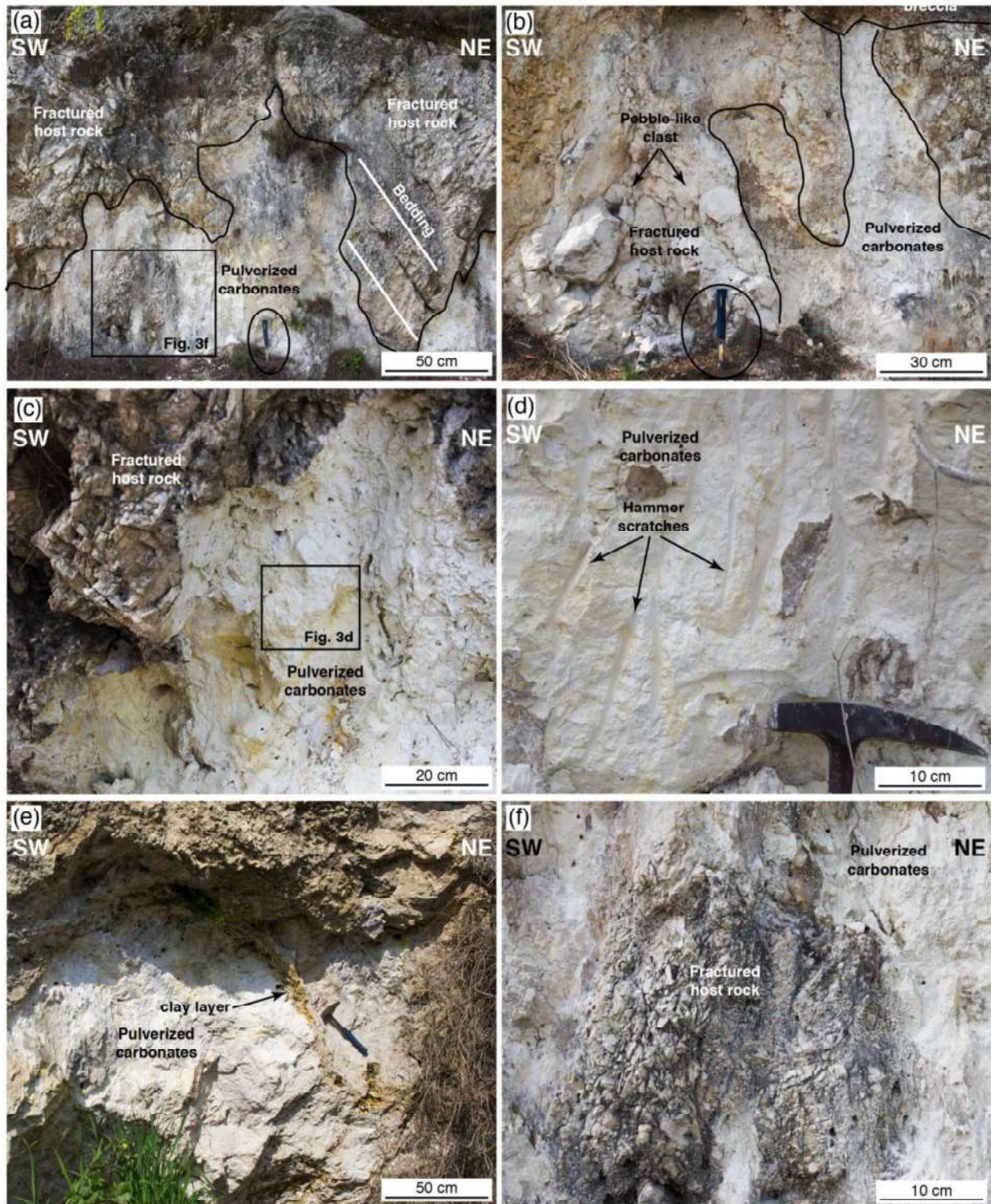
741

742 **Figure 2.** Exposure scale photographs (see also Videos S1-S4 and Virtual Outcrops S1-  
 743 S4). **(a, b)** Panoramic views of the pulverized dolostones showing domal and chimney-like  
 744 structures (pulverized pockets in the text) within bedded dolostone. Note the unconformity  
 745 between the carbonates and the overlying Quaternary slope debris deposits. Three Schmidt

746 polar plots (lower hemisphere; Table S3) in (a) show, from left to right, attitudes of bedding  
747 surfaces, normal faults, and joints (represented as contours to joint poles), respectively,  
748 measured along the studied exposure. **(c, d)** Pockets of pulverized dolostones where  
749 primary structures such as bedding are still preserved although finely pulverized.

750





751

752 **Figure 3.** Exposure scale photographs (see also Videos S1-S4 and Virtual Outcrops S1-  
 753 S4). **(a)** Pockets of pulverized dolostones embedded within highly fractured dolostone beds.  
 754 **(b)** Pulverized dolostones with preserved pebble-like clasts of host rock. **(c)** Boundary  
 755 between the pulverized dolostones and the fractured host rock. **(d)** Detail of pulverized

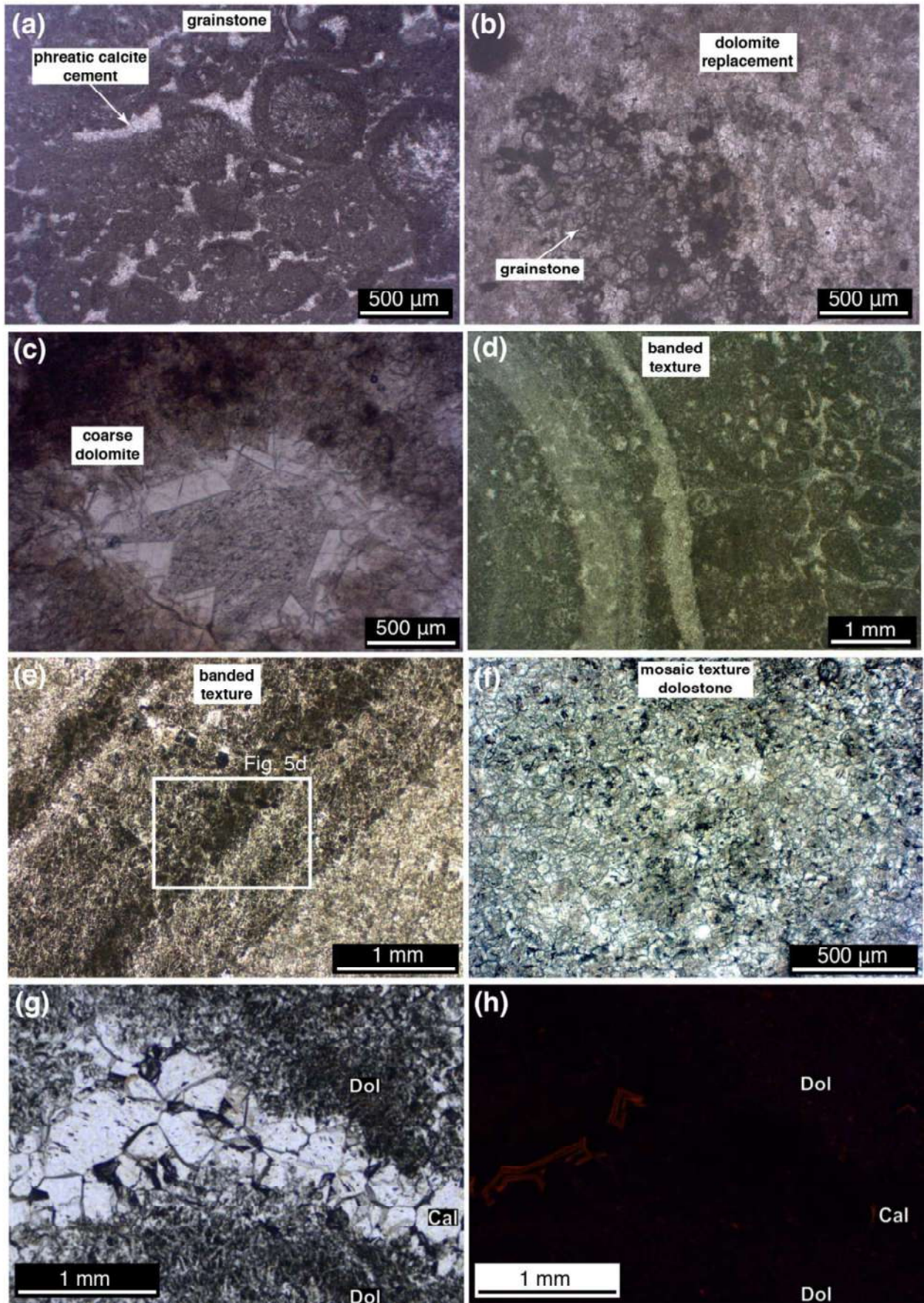
756 dolostones showing scratches created by the hammer to test the physical status of the rock.

757 **(e)** Antiformal clay-rich layer at the top of a pocket of pulverized dolostones. **(f)** Lens of highly

758 fractured host rock preserved within pulverized dolostones.

759

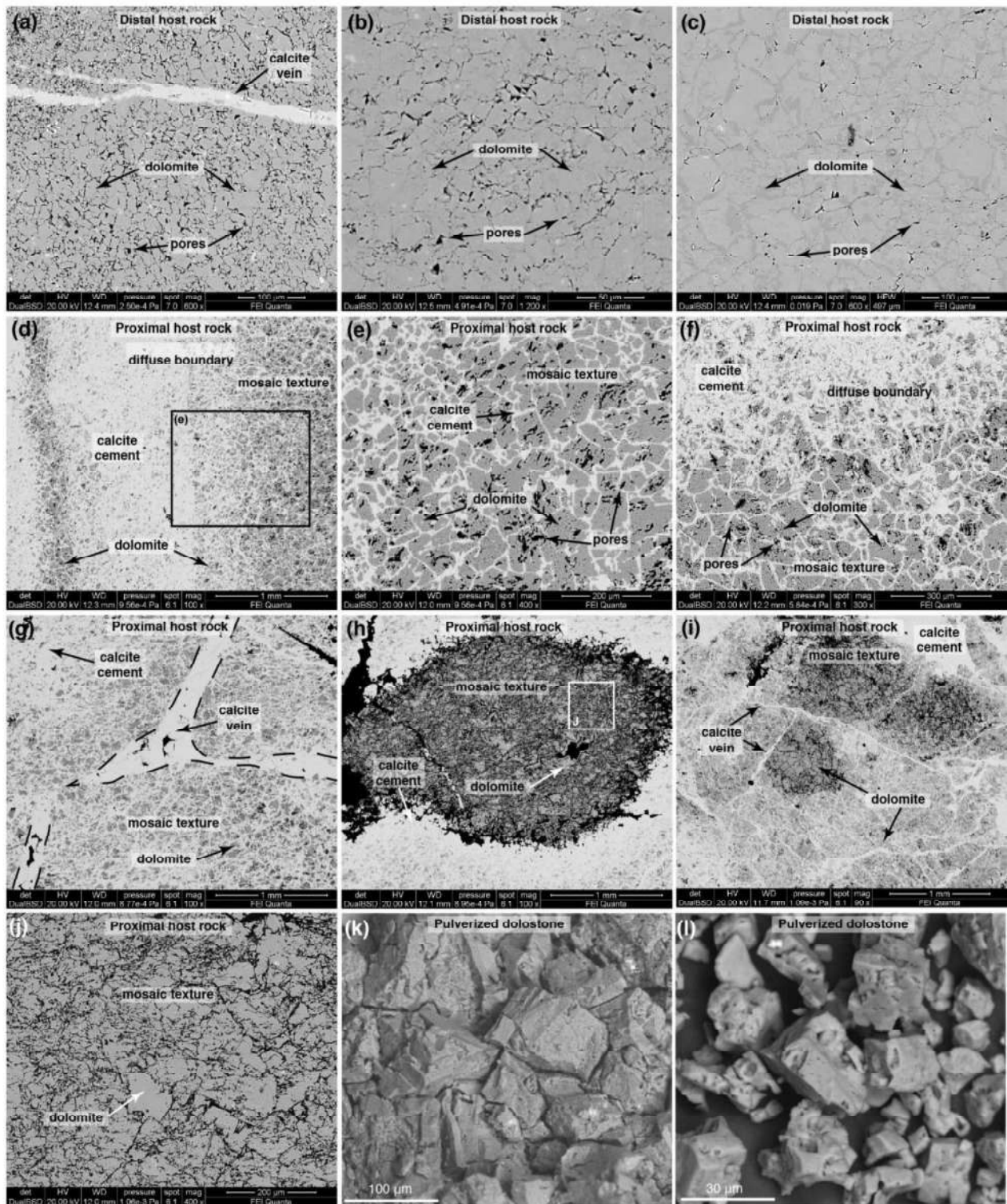




761 **Figure 4.** Microscopic photographs (see also Figs. S1-S4). **(a,b)** Distal carbonate host rock  
762 showing primary depositional features and evidence of diagenetic dolomitization. **(c)** Coarse  
763 secondary dolomite filling a void within distal carbonate host rock. **(d)** Proximal fractured  
764 host rock collected close to the pulverized dolostones, showing a banded texture. **(e)** Detail  
765 of banded texture showing fine-grained dolomite crystals. **(f)** Mosaic or crackle-like texture  
766 within the fine-grained dolomite crystals. **(g,h)** Calcite crystals filling a fracture and showing  
767 a dull red zoned luminescence color.

768



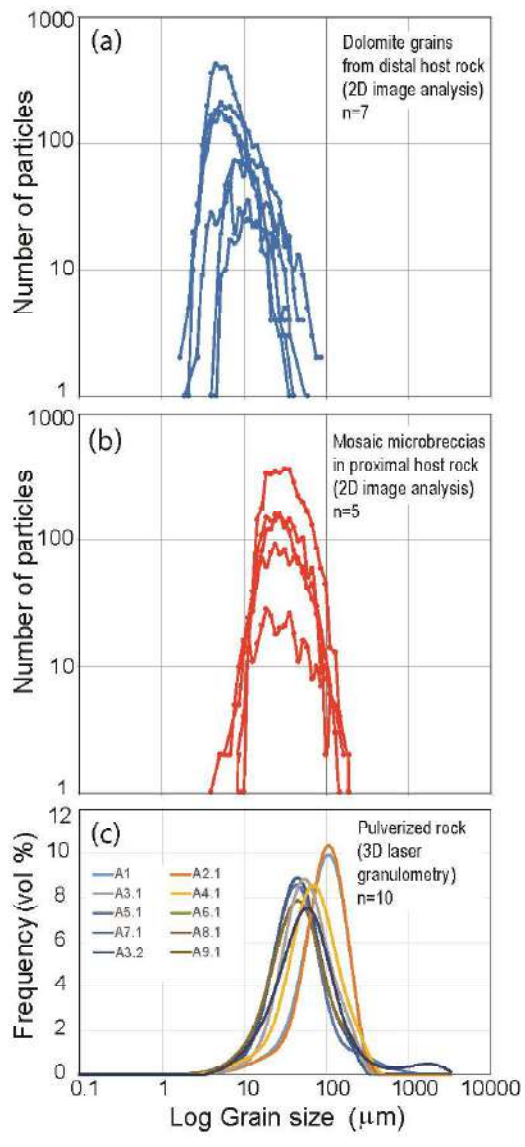


769

770 **Figure 5.** Microscopic photographs (see also Figs. S1-S4). (a-c) Microscale texture of the  
 771 distal carbonate host rock showing fine-grained dolomite crystals cut, in (a), by a calcite filled  
 772 vein. (d) Proximal host rock showing a banded texture with alternating bands made of fine  
 773 dolomite grains cemented by microcrystalline calcite. (e,f) Details of the fine dolomite grains

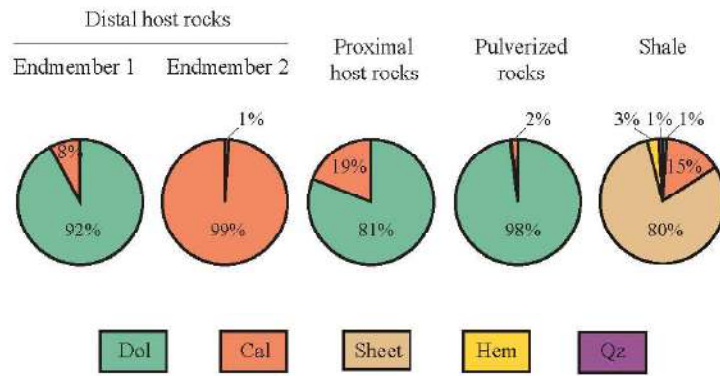
774 showing a mosaic or crackle-like texture with sharp grain boundaries (e) and a diffuse  
775 boundary between the dolomite grains and the microcrystalline calcite (f). **(g)** Calcite filled  
776 vein cutting the banded texture. **(h,i)** Proximal host rock showing lenses of fine dolomite  
777 grains with a crackle-like texture, sharp grain boundaries, and lack of microcrystalline calcite  
778 between the crystals. Compare these microphotographs with figure S2d in [Coppola et al.,](#)  
779 [\(2021\)](#). **(j)** Detail of fine dolomite grains showing a crackle-like (or masaic) texture and lack  
780 of microcrystalline calcite between the grains. **(k,l)** Details of the pulverized and incohesive  
781 dolostones characterized by fine dolomite grains with rhomboidal shapes and sharp  
782 boundaries.

783

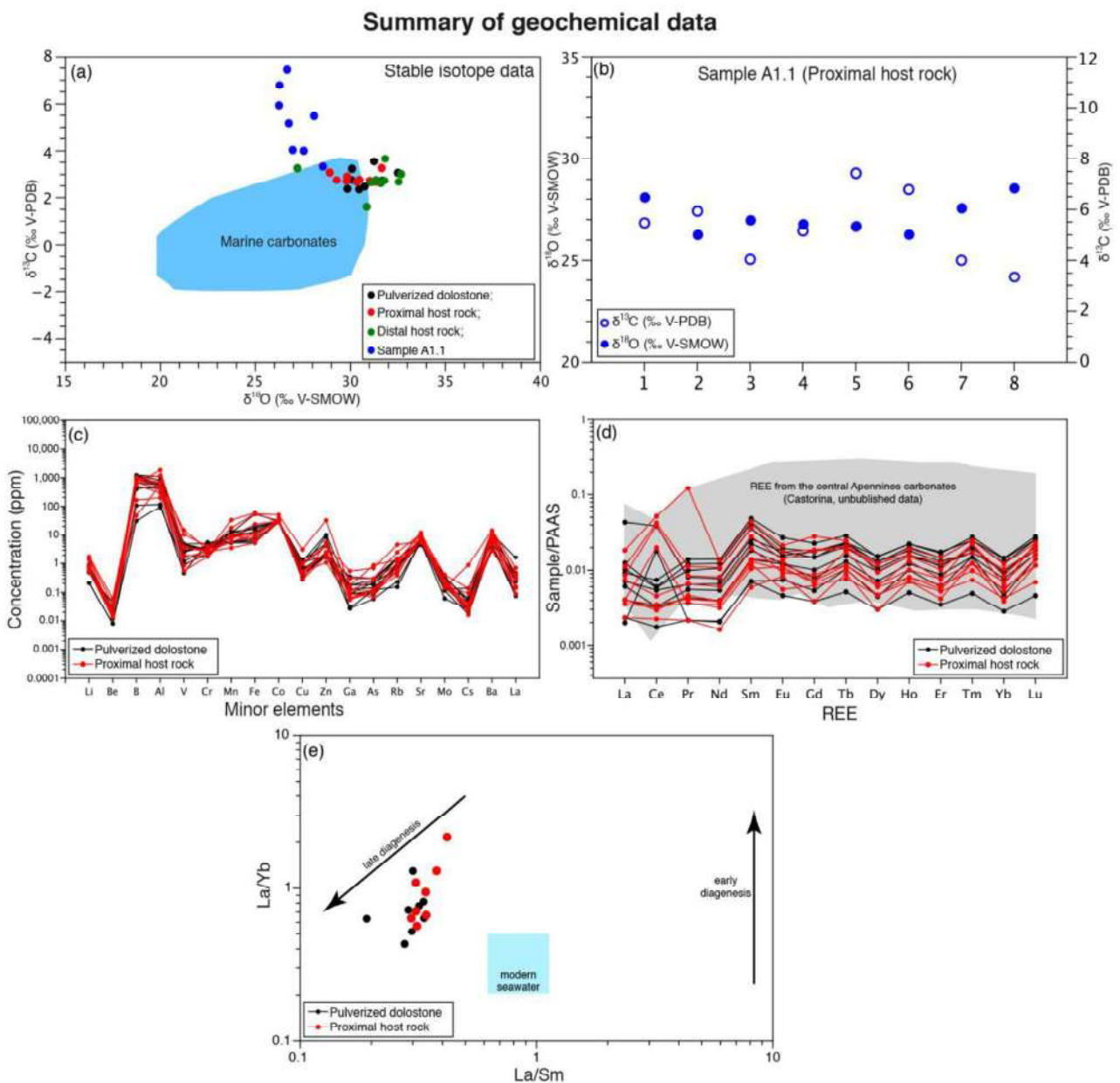


785 **Figure 6.** Grain size distributions (see also Figs. S5-S18 and Tables S4-S5). **(a)** Dolomite  
786 grains (i.e. crystals) from distal host rock (2D analysis). **(b)** Dolostone grains (mostly crystal  
787 aggregates, more rarely single crystals) from cemented crackle breccias in the proximal host  
788 rock (2D analysis). **(c)** Dolostone grains (mostly crystal aggregates, more rarely single  
789 crystals) from incohesive pulverized pockets of rocks (3D analysis).

790



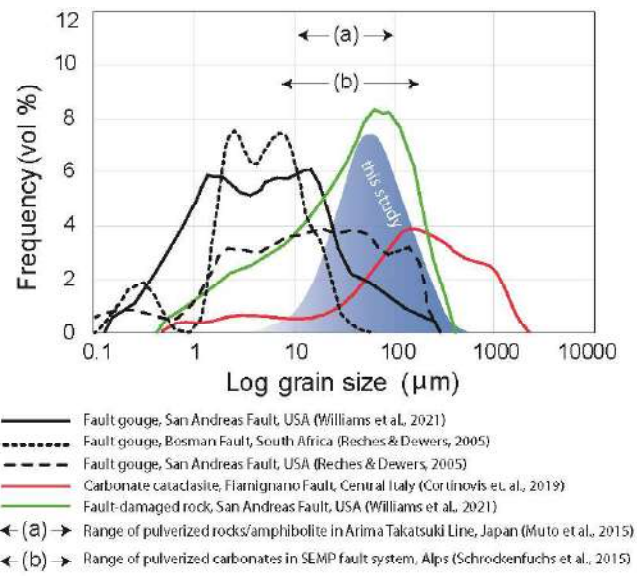
792 **Figure 7.** X-ray semiquantitative analysis of distal (e.g. Figs. 4a-4c) and proximal (e.g. Figs.  
 793 5d-5i) carbonate host rocks, pulverized rocks (e.g. Figs. 5k and 5l), and shales (or clay-rich  
 794 layers; e.g. Fig. 3e) interbedded with dolostone layers (Table S6). Dol-dolomite, Cal-calcite,  
 795 Sheet-Sheet silicate, Hem-hematite, Qz-quartz. Numbers refer to average values.  
 796



797  
 798 **Figure 8.** Geochemical data (Tables S7 and S8). (a) Diagram showing  $\delta^{13}\text{C}$  vs.  $\delta^{18}\text{O}$  values.  
 799 Note that pulverized carbonates have the same  $\delta^{13}\text{C}$  and  $\delta^{18}\text{O}$  values of those from distal

800 and proximal host rocks (bulk analyses). Micro-subsamples (punctual analysis) of calcite  
801 precipitates from sample A1.1 (Fig. S19; proximal host rock) show a large variability of  $\delta^{13}\text{C}$   
802 values and  $\delta^{18}\text{O}$  values lower than those of all other samples. **(b)** Diagram showing  $\delta^{13}\text{C}$   
803 and  $\delta^{18}\text{O}$  values vs. the sampling distance along the microscale transect (sample A1.1; Fig.  
804 S19). **(d)** Diagram for the concentration of minor elements. **(e)** REE concentration vs.  
805 Sample/PAAS showing that all the analyzed samples (pulverized carbonates and host  
806 rocks) are in the range of REE value or marine carbonates of the central Apennines (bulk  
807 chemical analysis). **(f)** La/Sm vs. La/Yb diagram showing that all samples have a late  
808 diagenetic imprint (bulk chemical analysis).

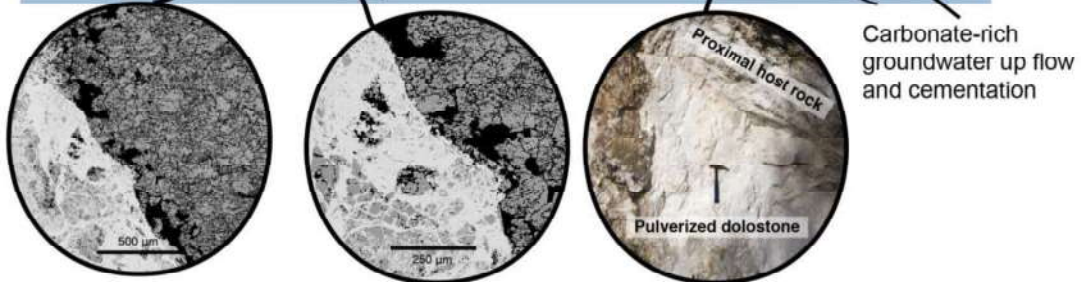
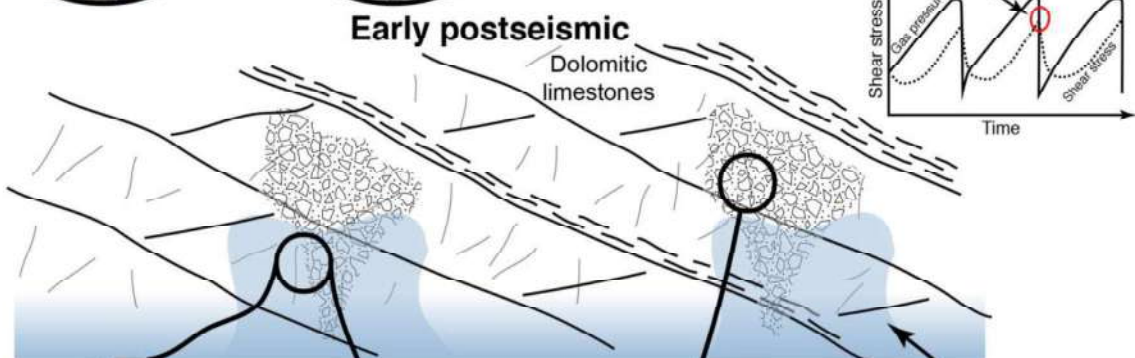
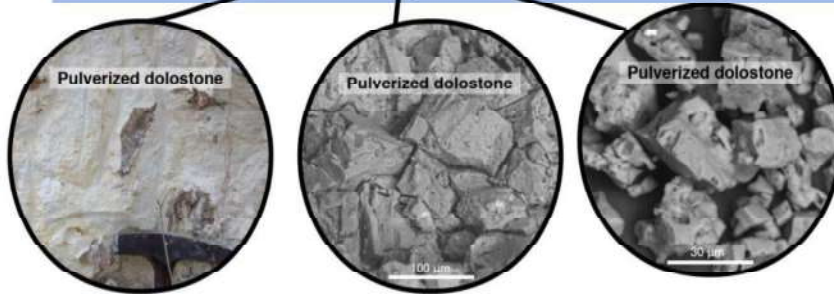
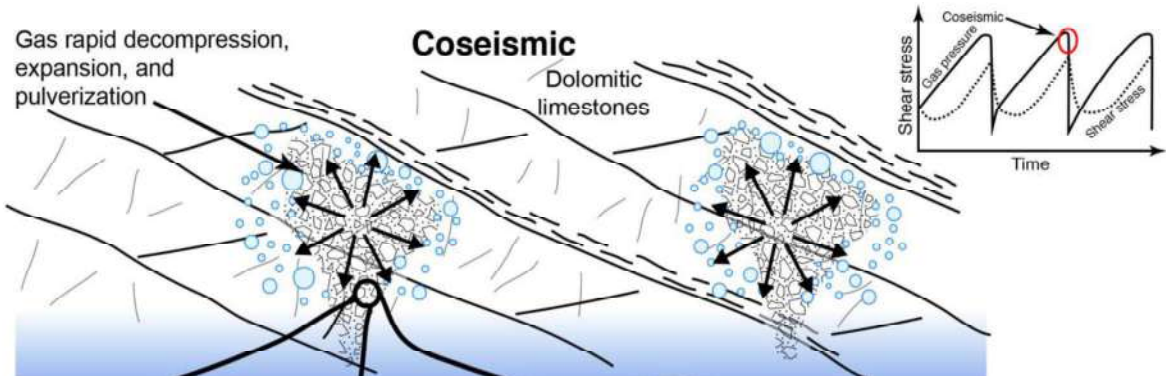
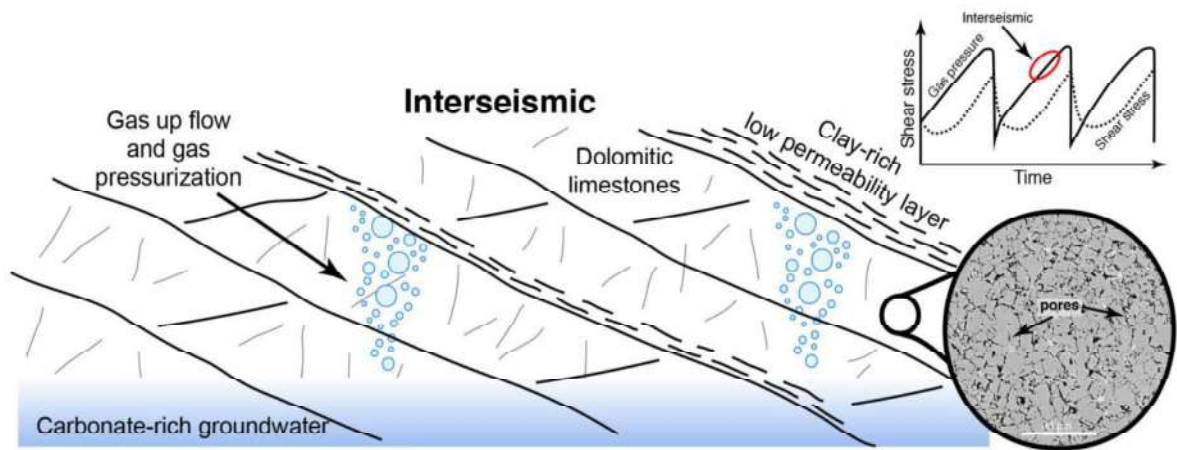
809





811 **Figure 9.** Comparison of grain size distributions between the pulverized rocks studied in this  
812 work (average curve in blue) and other fault-related pulverized rocks from the San Andreas  
813 Fault in California ([Reches and Dewers, 2005](#); [Williams et al., 2021](#)), the Salzach-Ennstal-  
814 Mariazell-Puchberg (SEMP) fault system in the Northern Calcareous Alps, Austria  
815 ([Schrockenfuchs et al., 2015](#)), the Bosman Fault in South Africa ([Reches and Dewers,](#)  
816 [2005](#)), and the Arima Takatsuki Line in Japan ([Muto et al., 2015](#)). For comparison, the grain  
817 size distribution curves of carbonate cataclasites and gouges from tectonically active  
818 localities in Italy ([Cortinovis et al., 2021](#)) are also plotted. Compared to fault-related  
819 cataclasites and gouges, the pulverized rocks have narrower grain size ranges and  
820 symmetrical, unimodal distributions.

821



823 **Figure 10.** Synthetic model of dolostone pulverization. During inter- to pre-seismic stages,  
824 CO<sub>2</sub>-rich gases accumulate and become pressurized in pockets of microporous dolostones  
825 at the top of a bicarbonate-rich aquifer. Likely during coseismic stages, the rock volume is  
826 rapidly decompressed and, where the permeability is sufficiently low to prevent a rapid  
827 escape of the gas from the rock, the trapped gas itself rapidly expand within the dolomitic  
828 rock, pulverizing it in situ. Soon after this stage, the decompression as well as the new  
829 porosity generated by the pulverization attracts the bicarbonate-rich waters, which rapidly  
830 degas (CO<sub>2</sub>) and precipitate a microcrystalline calcite cement that fossilizes the newly  
831 pulverized rock forming a cemented micro-mosaic or micro-crackle breccia. The  
832 cementation is so rapid that forms a sort of impermeable halo around the pocket of  
833 incoherent pulverized dolostone, preventing its cementation.

834